DIPARTIMENTO DI INGEGNERIA DELL'INFORMAZIONE,
ELETTRONICA E TELECOMUNICAZIONI

Corso di Laurea Magistrale in Ingegneria Elettronica

Stripper foil characterization from beam energy measurement in the Low Energy Ion Ring at CERN

Supervisor:
Prof. **Andrea Mostacci**

CERN Supervisor:
Dr. **Nicolò Biancacci**

Candidate:
Phani Deep Meruga

Matricola **1876754**

CERN-THESIS-2022-381
/ /2022

Academic year 2021/2022

Contents

List of Figures

List of Acronyms

CERN - European Organization for Nuclear Research

LEIR- Low Energy Ion Ring

LHC - Large Hadron Collider

LINAC - Linear Accelerator

PS - Proton Synchrotron

SPS - Super Proton Synchrotron

ATLAS - A Toroidal LHC apparatus

ALICE - A Large Ion Collider Experiment

CMS - Compact Muon Solenoid

LHCb - Large Hadron Collider beauty

TeV - Tera electron volt

GeV - Giga electron volt

MeV - Mega electron volt

BPM - Beam Position Monitor

DC - Debuncher Cavity

RC - Ramping Cavity

QGP - Quark-Gluon Plasma

RF - Radio Frequency

HCI - Highly Charged Ions

FFT - Fast Fourier Transform

“Failure will never overtake you if your determination

to succeed is strong enough”

- *Dr. A.P.J. ABDUL KALAM*

Abstract

The Linear Accelerator 3 (LINAC3) and the Low Energy Ion Ring (LEIR) at the European Organization for Nuclear Research (CERN) constitute the first stage of acceleration of Pb ion beams towards the Large Hadron Collider (LHC). In LINAC3, different stripper foils are strategically placed to maximize the beam transmission along the linac and the beam lifetime in the downstream machines. On one hand, the stripper foils play a crucial role in producing highly charged ions by stripping away electrons, thus preparing the ions for injection into other accelerators. On the other hand, as the ion beam passes through the foils over time, it significantly affects their stripping efficiency, potentially affecting the overall performance of the downstream machines. This thesis introduces an innovative method to study the performance evolution of the stripper foils. This is accomplished by means of longitudinal Schottky measurements performed in LEIR at injection, while tuning the phase properties of the Ramping cavity (RC) and the Debuncher cavity (DC) in LINAC3. By varying the phases of the RC and DC, it is possible to measure and control the energy spread of the beam in different operational conditions. Moreover, when systematically recording mean and standard deviation of the beam energy in LEIR over time, one can observe the evolution of the stripper foils performance and identify potential performance loss. Energy measurements are compared with simulations, allowing for a deeper understanding and providing means to correct possible energy deviations in advance. Furthermore, an online monitoring tool has been developed to continuously scan and record energy measurements automatically. This approach facilitates the timely foil replacement, thereby preventing beam intensity loss and performance loss in the ion injector chain.

Acknowledgments

The research work performed is part of my Final Thesis for a Master's Degree in Electronics Engineering at the Sapienza University of Rome. First of all, I would like to devote this thesis to my mom and dad for their selfless love, affection and giving me the best education in my life. I am sure they will shower their blessings and see my success from the heaven. I would like to thank my uncle Mr. Pradeep Kumar Meruga for his guidance, emotional support, looking after my financial needs and standing beside me in tough times throughout my educational career.

I would like to extend my sincere gratitude towards my university professor Dr. Andrea Mostacci for his continuous support in my academics at the university and also for his valuable suggestions throughout my research work, enlightening and helping me to pursue my career in the field of particle accelerators. Thank you, Professor, for standing beside me as a guardian in my life.

Next, I would like to thank European Organization for Nuclear Research (CERN), especially my supervisor Dr. Nicolo Biancacci from Coherent Effects and Instabilities section for trusting and providing me with the greatest opportunity to work under him and complete my research work with great satisfaction. I am grateful to be supervised under him where I was taught innovative ways to solve problems and was able to receive continuous assistance throughout my research. Special thanks to my section leader Dr. Giovanni Rumolo, deputy Beams Department head Dr. Richard Scrivens, Dr. Reyes Alemany Fernandez, Dr. Carlo Zannini and the whole LINAC3 team for providing me with their valuable insights that helped to carry out my work with ease and perfect.

Further, I would like to thank my colleagues Chiara, Sofia, Enrico, Alessandro, Sebastien and Filippo for assisting me during work and exploring the city of Geneva together. Finally, I would like to express my gratitude to my friends Mariangela and Satya for their unconditional support, who stood beside me during tough times and guiding me towards making right decisions in my life.

Chapter – 1

Introduction

The European Organization for Nuclear Research (CERN) is an international organization that operates the largest particle physics laboratory in the world. It is located in the northwest suburbs of Geneva on the Franco-Swiss border. CERN's main purpose is to provide a collaborative environment for research in particle physics, which is the study of the fundamental nature of matter and energy. CERN was founded in 1954 and is currently home to more than 10,000 scientists, engineers, and other personnel from over 100 different countries. One of the main goals at CERN is to conduct research on the properties of nuclei and the structure of atomic nuclei using heavy ions which are dedicated to the heavy-ion physics programme and study the properties of protons and neutrons in a nucleus and the way they interact with each other. Its facilities include the Large Hadron Collider (LHC), which is the world's most powerful particle accelerator, and several other particle accelerators such as Super Proton Synchrotron (SPS), the Proton Synchrotron (PS), the Low Energy Ion Ring (LEIR), the Linear Accelerator 3 (LINAC3) and detectors that includes ALICE, ATLAS, CMS, LHCb.

CERN's most notable achievements was the discovery of the Higgs boson in 2012, which was a major step forward in our understanding of the fundamental nature of the universe. CERN also plays a key role in the development of new technologies. CERN is funded by its member states and also receives support from international organizations and private sponsors. It is a non-profit organization and its research is made available to the public through scientific publications and public outreach programs.

1.1 CERN accelerator complex

The CERN accelerator complex [1] as shown in figure 1, includes a chain of injectors interconnected between each other through the transfer lines. The main aim of the injectors is to accelerate ions (atoms with a positive charge) or protons to extremely high energies, allowing them to be used in various scientific experiments and research projects. The ion injector chain at CERN consists of several different accelerators, each of which serves a specific purpose in the overall process of accelerating ions. The first accelerator in the chain is the Linear accelerator 3 (LINAC3), which is used to produce heavy ions such as lead, accelerate the ions to an energy of 4.2 MeV/u and then strip the electrons to reach a higher ion charge state before passing the ion beam to the next injector. The

LINAC3 is followed by the Low Energy Ion Ring (LEIR), which is a circular accelerator that uses electron cooling technique for stacking of the incoming ion pulses and further increases the energy of the ions to 72 MeV/u. These ions are then passed through a series of successive accelerators that include Proton Synchrotron (PS) and Super Proton Synchrotron (SPS), each of which increases the energy of the ions until they reach the desired energy level. The Ion beam then reaches the LHC in form of bunches where the beam in one tube rotates in clockwise direction and the beam in the second tube in the anti-clockwise direction making the two beam to rotate in opposite directions. Then the two circulating ion beams with the help of RF cavities reach the maximum energy of 2.75 TeV/u per ion beam and are made collided inside the four detectors (ALICE, ATLAS, CMS and LHCb) where the total energy at the centre of collision stands at 5.5 TeV/u.

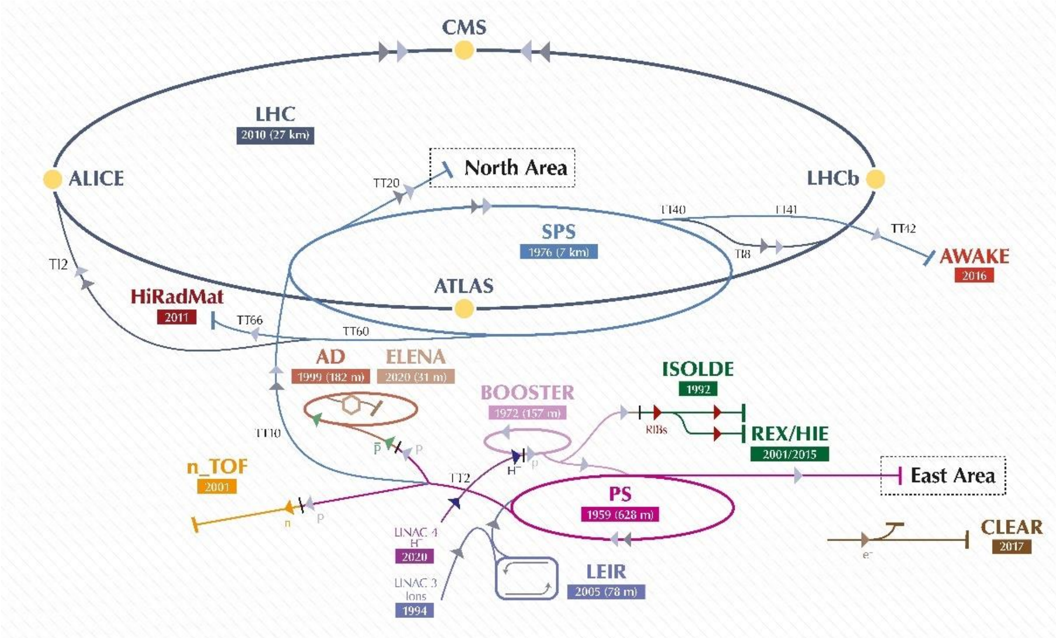

Figure 1: The CERN accelerator complex. [1]

ALICE (**A** **L**arge **I**on **C**ollider **E**xperiment) is designed to study the properties of matter at extreme temperatures and densities, specifically the quark-gluon plasma (QGP) which is a plasma of quarks and gluons, the fundamental building blocks of protons and neutrons that is thought to have existed in the early universe a few microseconds after the Big Bang. The ALICE experiment uses the LHC to collide lead ions (heavy atomic nuclei) at an energy of about 5.5 TeV per nucleon. These collisions create extremely high temperatures and densities, reaching up to a million times the temperature of the center of the sun and several times the normal density of nuclear matter.

ATLAS (**A** **T**oroidal **L**HC **A**pparatu**S**) is designed to study a wide range of phenomena in particle physics, including search for new particles and forces that may be beyond the Standard Model of particle physics, the current theory that describes the fundamental structure of the universe. This includes the search for the Higgs boson, a particle that was predicted by the Standard Model and was discovered by the ATLAS experiment at the LHC in 2012. The Higgs boson is thought to be responsible for giving other particles mass, and its discovery was a major milestone in the field of particle physics. In addition to the search for new particles, the ATLAS experiment is also used to study the properties of known particles, such as quarks, leptons, and gauge bosons. This includes the study of the strong and weak nuclear forces, which are the fundamental forces that govern the interactions between subatomic particles.

The **CMS** (**C**ompact **M**uon **C**ollider) is used to measure the properties of collided particles that are produced at small angles relative to the beam direction. The CMS detector consists the Calorimeter and the Muon Chambers, which are used to measure the energy and momentum of particles and to identify muons (a type of heavy lepton). The main achievement of CMS includes the discovery of the Higgs boson, along with ATLAS experiment in 2012.

LHCb (**L**arge **H**adron **C**ollider **b**eauty) is designed to study the properties of beauty quarks (b-quarks) and their antimatter counterparts, anti-b quarks. These particles are of particular interest to scientists because they are produced in large quantities in high-energy particle collisions, and they are thought to play a role in the asymmetry between matter and antimatter in the universe. The detector is positioned at one of the LHC's interaction points, where the beams of protons collide, and it is designed to detect and measure the properties of particles produced in these collisions. In addition to the study of b-quarks, the LHCb experiment is also used to study the properties of other particles, such as charm quarks.

1.2 Heavy Ion programme at CERN

The heavy ion programme at CERN (European Organization for Nuclear Research) is a research initiative focused on the study of collisions between heavy ions, or atomic nuclei with a large number of protons and neutrons. These collisions are used to recreate the conditions of the early universe, just after the Big Bang, in order to understand the fundamental properties of matter and the fundamental forces that govern it. The programme began in the early 1980s with the creation of the Super Proton Synchrotron (SPS), a particle accelerator that was used to collide protons and other lighter ions. In the 1990s, the SPS was upgraded to become the SPS Heavy Ion Accelerator, which allowed for the acceleration and collision of heavier ions. The heavy ion programme has since expanded to include the Large Hadron Collider (LHC), a much larger and more powerful accelerator that was built in the 2000s to collide protons and heavy ions at even higher energies. The main goal of the heavy ion programme at CERN is to study the quark-gluon plasma (QGP), a state of matter that is thought to have existed in the early universe just after the Big Bang.

The QGP is a type of plasma that is composed of quarks and gluons, the fundamental building blocks of matter, which are normally bound together inside protons and neutrons. In the QGP, these quarks and gluons are thought to be "unbound" and able to move freely, much like the electrons in a plasma. The QGP is thought to have existed for only a brief period after the Big Bang, before the universe cooled down enough for the quarks and gluons to bind together again and form protons and neutrons. This transition, known as quark confinement, is one of the fundamental mysteries of modern physics, and the heavy ion programme at CERN is designed to help us understand it.

To study the QGP, researchers at CERN use the SPS Heavy Ion Accelerator and the LHC to collide heavy ions at very high energies. These collisions create extremely high temperatures and pressures, which are thought to be similar to those that existed in the early universe just after the Big Bang. When the ions collide, they create a "fireball" of hot, dense matter that expands outward in all directions. This expanding fireball is thought to be similar to the QGP, and researchers can study it using a variety of different experimental techniques. For example, they can measure the energy and momentum of the particles produced in the collisions, as well as the temperature and pressure of the fireball itself. They can also study the properties of the quarks and gluons within the fireball, such as their masses and how they interact. One of the main challenges of the heavy ion programme at CERN is understanding the QGP's fundamental properties and how it behaves. For example, researchers are interested in understanding how the quarks and gluons within the QGP interact with each other and how they flow and behave under different conditions. They are also interested in understanding how the QGP cools down and transitions back into ordinary matter, and what happens to the quarks and gluons during this process.

To answer these questions, researchers at CERN use a variety of different experimental techniques and tools. For example, they use detectors such as the ALICE detector, which is designed specifically to study heavy ion collisions at the LHC. The ALICE detector consists of a large number of sensors and detectors that can measure the energy, momentum, and other properties of the particles produced in the collisions. Overall, the heavy ion program at CERN is a major international research effort that is helping to advance our understanding of the fundamental nature of matter and the universe.

1.3 Overview of LINAC3 at CERN

LINAC 3 also known as linear accelerator 3 [2] [3] is a key component in the operation of many particle accelerators and synchrotron facilities at CERN. It is used to accelerate heavy ions to very high energies, which are then sent to the following synchrotrons (LEIR, PS, SPS) to eventually reach LHC or serve fixed target experiments. LINAC 3 consists of a series of cavities or radio frequency (RF) structures that are connected in series to form a long, linear accelerator. LINAC3 is an essential part of the LHC, the world's largest particle accelerator. The ions that are accelerated in Linac 3 to an energy of 4.2 MeV/u are used to collide with each other in the LHC, allowing scientists to study the interactions and behaviours of these subatomic particles. It is an important component of CERN's research infrastructure and plays a crucial role in the organization's efforts to advance our understanding of the fundamental nature of the universe and the forces that govern it.

Below figure 2 depicts the machine layout of the LINAC3 starting from the source to the right side and through the RF cavities present in the tanks and the Linac to Filter (ITF) line. In LINAC3, the most common ion used is lead as a beam source for particle acceleration, which has several unique properties that make it ideal for certain types of experiments.

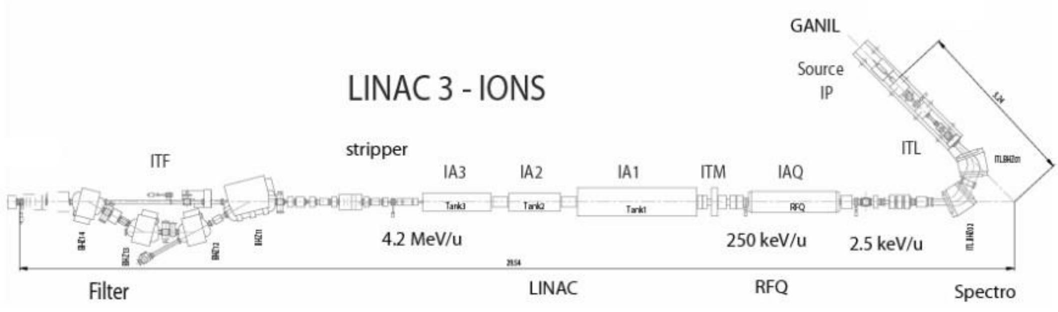

Figure 2: Schematic layout of the LINAC3.

The process begins with a beam of lead ions that are generated through a process called "ionization." This involves stripping the outer electrons from lead atoms to create a beam of positively charged ions. This is usually done in an ion source chamber, where the lead atoms are vaporized and then bombarded with high-energy electrons. The electrons collide with the atoms and knock off the outer electrons, resulting in the formation of lead ions [3]. The ionized lead atoms are then extracted from the source where they are needed to be transported and focused into a beam. This is done using several components such as lenses, deflection plates, and magnetic fields. The ions are first accelerated through an electric field, which gives them a boost in energy. Then, they are passed through a series of lenses, which focus and shape the beam into a more defined and concentrated stream. The beam is focused using a variety of techniques. One common method is the use of quadrupole magnets, which preserve the ions beam size along the accelerating structure. Other techniques, such as solenoids and dipoles, can be used to bend the path of the ions in a controlled manner, allowing them to be directed toward a specific target or experiment. After the lead ions have been produced and focused into a beam, they are ready to be injected into the LINAC3. This is done using a beam transport system, which consists of a series of vacuum-sealed tubes and pipes that guide the beam to the accelerator. The beam is injected into the accelerator through an injector port, where it is further accelerated to the desired energy level.

It is a complex process that requires precise control and careful manipulation of the ions to ensure accurate and effective results.

Now the focused beam is directed toward the acceleration. In a LINAC, the particles are accelerated through a series of RF cavities, which are arranged linearly along the length of the accelerator. The operation of an RF cavity in a LINAC can be understood by considering the interaction between the charged particles and the electromagnetic fields inside the cavity. When an RF cavity is energized with an alternating electric field, the charged particles passing through the cavity will experience a force that pushes them in the direction of the electric field. The magnitude of this force is determined by the strength of the electric field, which is determined by the voltage applied to the cavity. As the charged particles pass through the cavity, they will also experience a force due to the magnetic field inside the cavity. The direction of this force will depend on the direction of the magnetic field and the direction of motion of the particles. The combination of the electric and magnetic forces acting on the particles causes them to follow a spiral path as they pass through the cavity. As the particles pass through successive RF cavities, they gain energy and are accelerated to higher velocities.

In LINAC3, the RF cavities [2] [3] are typically arranged in a series, with each cavity operating at a slightly higher frequency than the previous one. This allows the particles to be accelerated to progressively higher energies as they pass through the series of cavities. These cavities generate an electromagnetic field that oscillates at a specific frequency. As the particles pass through the cavities, it interacts with the electromagnetic field and is accelerated to higher energies. This process is repeated as the particles pass through successive cavities until they reach the desired energy level. The RF cavities in the LINAC3 are typically driven by high-power RF amplifiers, which are used to generate the alternating electric and magnetic fields inside the cavities. The RF amplifiers are typically powered by a high-voltage power supply, which provides the necessary electrical energy to drive the RF cavities. These cavities are usually made of copper and are shaped like cylinders, with an outer radius of about 30 cm and a length of about 1.5 m. They are arranged in a straight line, with a gap of about 1 m between each cavity. Linacs are usually divided into two main types: radio frequency (RF) linacs and electrostatic linacs. RF linacs use alternating current (AC) electric fields to accelerate the ions, while electrostatic linacs use direct current fields. RF linacs are generally more efficient and easier to operate, but they are limited to lower energy acceleration compared to electrostatic linacs. In addition to these basic elements, LINAC3 also includes several other components and systems that are used to optimize the performance of the accelerator. For example, beam diagnostic systems are used to monitor the properties of the ions as they pass through the accelerator, allowing operators to adjust the accelerator parameters as needed to maintain optimal performance. Other systems, such as vacuum pumps and cryogenic cooling systems, are used to create and maintain the high vacuum and low-temperature conditions that are necessary for the operation of the machine.

1.4 Overview of LEIR at CERN

The Low Energy Ion Ring (LEIR) [2] is a circular particle accelerator located at the European Organization for Nuclear Research (CERN) in Geneva, Switzerland. It is the first ion synchrotron accelerator along the ion injection chain of accelerators at CERN. It is used to accelerate, store ions, and deliver high-brightness bunches to LHC. The basic shape of the LEIR as shown in figure 3 is square with four bending sections consisting of large dipoles to deflect the beam by 90° and has four straight sections which can be seen clearly from figure 4 describing the LEIR machine layout [3] [4] that consists of four straight sections namely Injection section ER.SS10, Electron cooling section ER.SS20, Kicker section ER.SS30, Extraction and RF section ER.SS40. The geometry of machine has a quasi-twofold periodicity system since the injection and cooling entail different lattice parameters in the respective straight sections. So, the injection section ER.SS10 and electron cooler section ER.SS20 are placed adjacent to each other. In order to foresee suitable optics of the machine, one quadrupole is placed per quarter of the machine in the cooling section i.e., straight section SS20, and in the opposite section i.e., straight section SS40. Therefore, the focusing and defocusing of the beam are produced by the triplets that are placed in the cooling section (SS20), extraction section (SS40), and by the doublets that are placed in the injection section (SS10), kicker section (SS30). Two RF cavities are installed in the dispersion vanishing section ER.SS40 in order to avoid the synchro-betatron resonances. Only a single RF cavity is used during the operation and the other cavity is used as a hot spare.

Electron cooling is a technique used to reduce the kinetic energy of ions in a beam. In LEIR, electron cooling is used to reduce the energy spread of ions as they circulate through the ring. This is accomplished by introducing a beam of electrons that are cooled to a very low temperature (tens of millikelvins) and then injected into the ion beam. As the ions and electrons pass through the ring, they interact via Coulomb forces, resulting in energy transfer from the ions to the electrons, thus decelerating the beam and adding it to the stack. This process is repeated multiple times as the ions circulate through the ring, resulting in a significant reduction in energy spread and an increase in beam brightness. In addition to reducing energy spread, electron cooling also helps to reduce emittance (the transverse size and shape of the ion beam), which is important for maintaining a high-quality beam during acceleration and extraction.

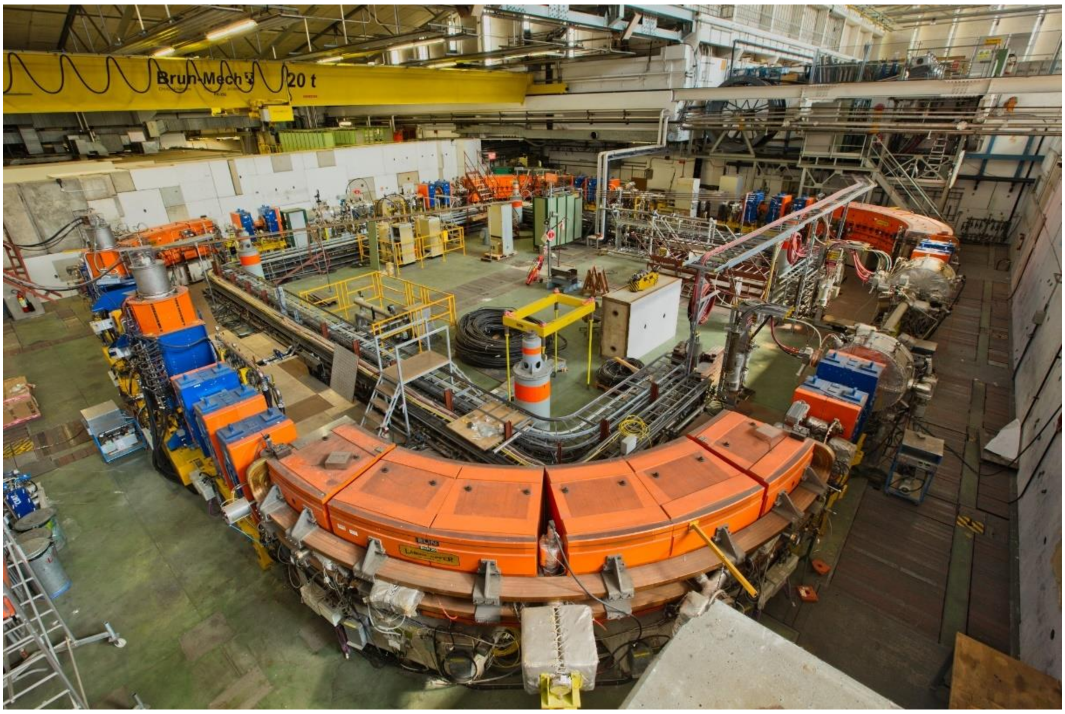

Figure 3: Low Energy Ion Ring (Top view)

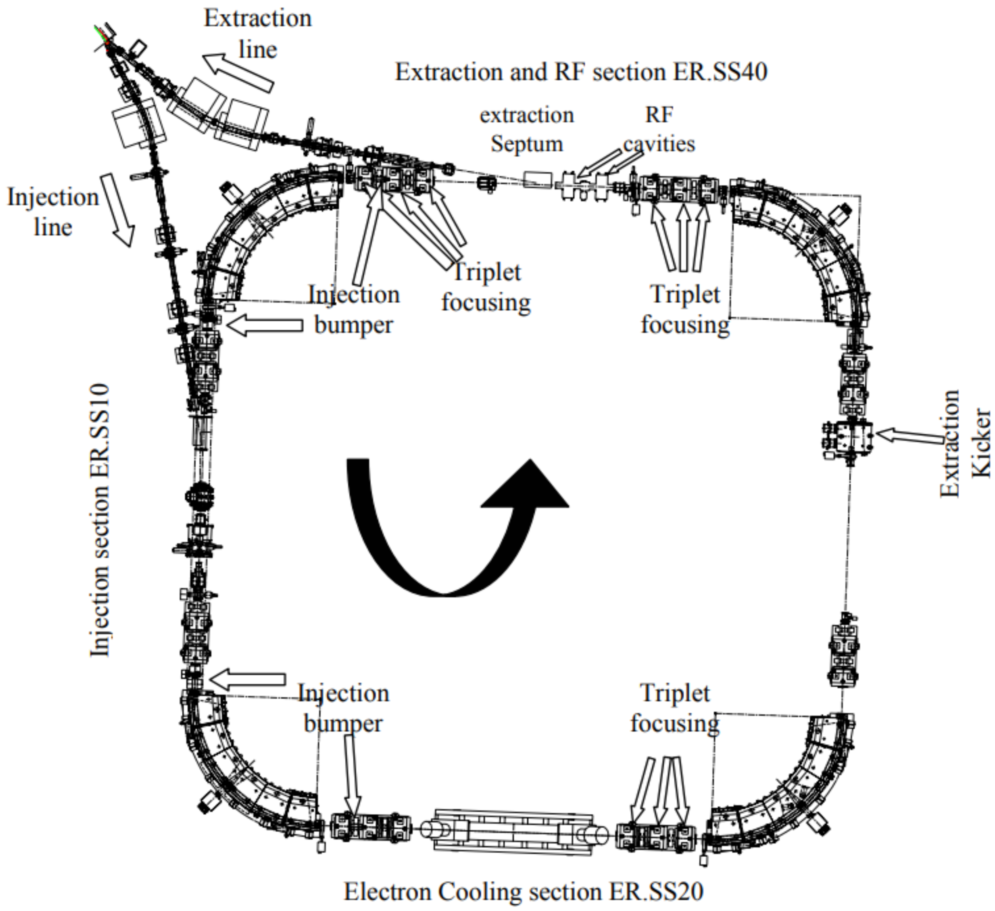

Figure 4: LEIR machine layout

RF cavities in an accelerator are typically made of copper and have a cylindrical shape with rounded ends. The frequency of the RF field within the cavity is determined by the geometry of the cavity and the type of particle being accelerated. The RF field must be carefully tuned to match the resonant frequency of the cavity to achieve optimal acceleration of the ions. In order to avoid any significant drawback from the optics design of the transfer line the beam is circulated within the machine in the counter-clockwise direction. Table 1 depicts the general parameters of the machine and further, the machine includes the correction dipoles, sextupoles, solenoids, dampers, beam diagnostic devices, etc.,

Parameter	Value
Circumference	78.54m
Relativistic beta	0.095(inj)-0.37(ext)
Gamma	1.0045(inj)
Revolution Frequency	0.36-1.42 MHz
Energy	4.2(inj)-72(ext)MeV/u
Q_H, Q_V	1.82, 2.72
Injection pulse	200µs 50µA
Ejection bunch	2*200ns 50mAp

Table 1: LEIR parameters

The main function of LEIR [2] [5] is to transform the incoming series of long (200µs), low-intensity ion pulses from LINAC3 to short (200ns), high-density bunches by using phase space cooling and ion accumulation. The phase space cooling is performed by electron cooling technique due to the fast-cooling time (<0.4s) at the injection energy of 4.2MeV/u and is better upon comparing with other techniques. Each received Pb^{54+} LINAC3 pulse is injected into LEIR by stacking over 70 turns. Once seven pulses are accumulated, cooled, and stacked one upon each other the electron cooling is turned off and followed by the adiabatic capture and acceleration of bunches to 72 MeV/u which is clearly shown in the below figure 5 and then sent to the Proton Synchrotron (PS) for further acceleration of the beam. The total length of the LEIR cycle is 3.6s.

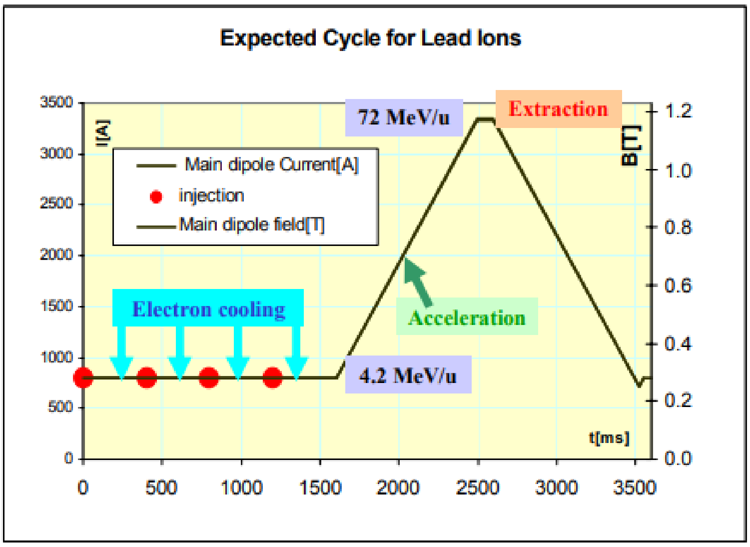

Figure 5: LEIR cycle for Lead ions

Below figure 6 (A) depicts the detailed information about the LEIR nominal cycle where the magnetic cycle that determines the beam energy within the machine is viewed in red colour with flat bottom until the start of ramping at 1.86s. The seven injections are taken place for the nominal cycle at the flat bottom between 0.2 to 1.7s with the electron cooler turned on. The total duration between the first injection and last injection is 1.3s so that the accumulation of ions, and stacking of every single injected pulse from LINAC3 happen which is indicated clearly. Therefore there is an increase in intensity of the whole beam. Then the electron cooler is turned off following the adiabatic capture of the beam. Next, the Radio Frequency cavities are turned on immediately for the acceleration of the beam where the injected beam with energy of 4.2 MeV/u is accelerated to 72 MeV/u during the ramping and follows the extraction of the accelerated beam at 2.87s and further sending it to the next accelerators in the chain through the transfer lines.

Below figure 6 (B) describes the detailed information of LEIR Early cycle which functions for only a single injection. Similar to nominal cycle the injection takes place at the flat bottom of the machine's magnetic cycle with the electron cooler turned on for 0.25s to have an adiabatic capture of the beam. Then the electron cooler is turned off and immediate start of the RF cavities takes place for the acceleration of the beam to a higher energy which is performed in ramping stage. Then the single injection beam with reduced intensity compared to nominal cycle is extracted at the flat top of the magnetic cycle and further transporting the beam to the next accelerators in the chain through transfer lines. The whole process from injection of the pulse to the extraction of the high energy beam is completed within 1.6s. This Early cycle is used in this frame of research work to perform measurements which are discussed later in this thesis.

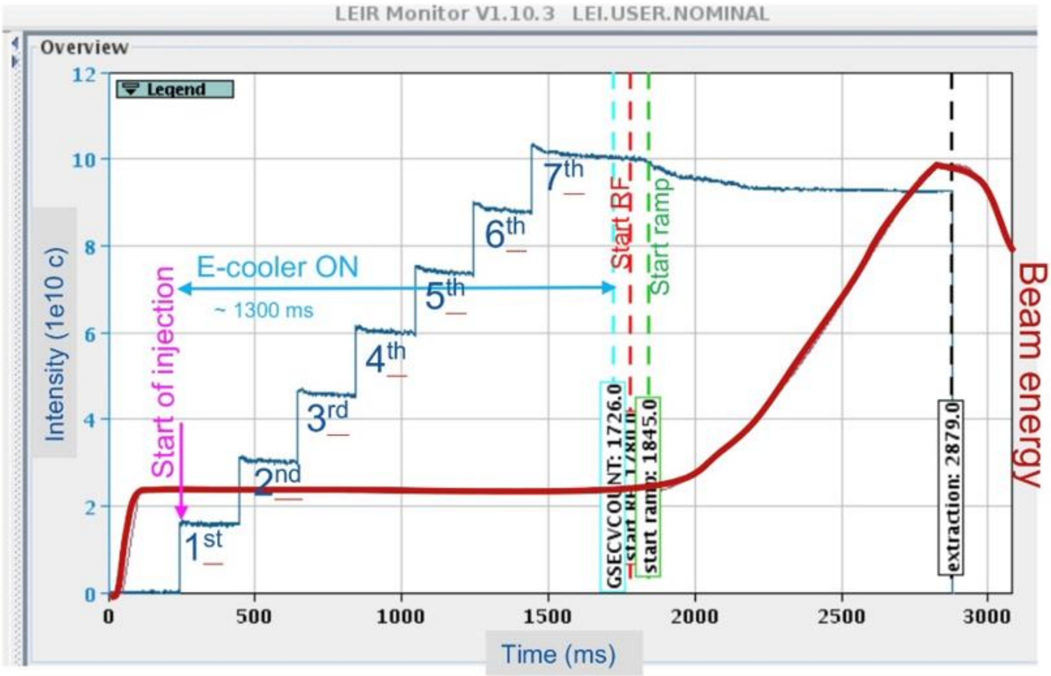

(A)

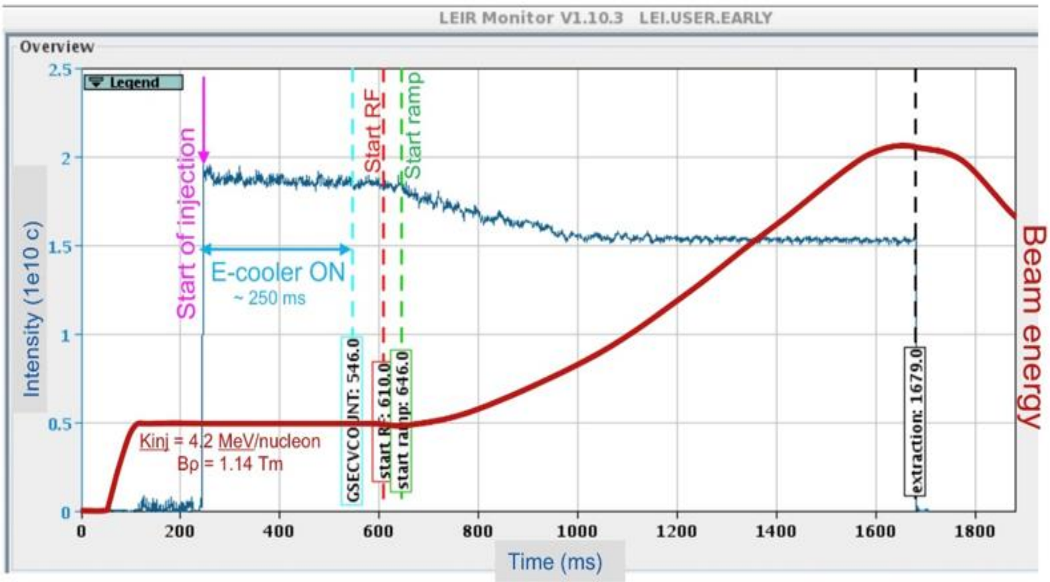

(B)

Figure 6: A shows the LEIR Nominal cycle [16] and B shows the LEIR Early cycle [16]

Chapter – 2

Beam Dynamics and Filter-Stripper line at LINAC 3

2.1 Particle Beam Dynamics

The dynamics of the ions in a LINAC are complex and involve both transverse and longitudinal motion. In this section, longitudinal beam dynamics of ions in a LINAC is discussed. Longitudinal beam dynamics refers to the motion of the ions along the direction of the beam, which is typically the same direction as the acceleration of the ions. The ions in a LINAC are typically accelerated to high energies over a relatively short distance, and as they gain energy, they also gain mass due to the relativistic increase in mass. This increase in mass can significantly affect the beam dynamics and must be taken into account in the design and operation of the LINAC. One of the key quantities that is used to describe the longitudinal beam dynamics is the energy gain per unit length, or gradient (k). The gradient is defined as the change in energy per unit length and is typically expressed in units of MeV/m. The gradient is an important parameter in the design of a LINAC, as it determines the length of the accelerator required to reach a given energy. The gradient is related to the electric and magnetic fields that are used to accelerate the ions. The electric field, E, accelerates the ions in the direction of the field, while the magnetic field, B, acts on the ions in a direction perpendicular to both the field and the velocity of the ions. The combination of these two fields results in the ions following a helical path as they are accelerated. The relationship between the gradient (k), electric field, and magnetic field is given by the below equation 2.1:

$$\mathrm{k} = \mathrm{eE}/(m_0c^2 + \mathrm{eE}/c^2) \tag{2.1}$$

where e is the charge of the ions, m_0 is the rest mass of the ions, c is the speed of light, and E is the electric field. The gradient can also be related to the phase advance, which is defined as the change in the phase of the ions' oscillation per unit length. The phase advance is related to the gradient through the equation 2.2:

$$k = \left(\frac{2\pi}{\lambda}\right) * (n - \cos{(\Phi)}) \tag{2.2}$$

where λ is the wavelength of the ions, n is the refractive index of the accelerating structure, and Φ is the phase advance. The phase advance is an important parameter in the design of a LINAC, as it determines the stability of the beam. If the phase advance is too large, the beam can become unstable and begin to oscillate, leading to a loss of beam intensity. On the other hand, if the phase advance is too small, the beam can become tightly focused, leading to a reduction in the beam current.

The dynamics of the ions in the beamline can be described by a set of equations known as the longitudinal beam dynamics equations that consists of the equation of motion, the energy conservation equation, the phase space equation, and the envelope equation. These four equations are sufficient to describe the longitudinal beam dynamics of ions in Linacs. These ions are typically confined to a narrow beamline and subjected to various forces as they are accelerated through the LINAC.

The first equation in the longitudinal beam dynamics is the equation of motion, which describes the acceleration of the ions due to various forces. This equation is given by Newton's second law, which states that the acceleration of an object is equal to the net force acting on it divided by its mass. In the case of an ion beam in a LINAC, the net force is the sum of the electric and magnetic forces acting on the ions. The electric force on an ion in an electric field is given by the Lorentz force law, which states that the electric force on a charged particle is equal to the product of the charge of the particle, the electric field, and the velocity of the particle. The electric field in a LINAC is typically produced by a series of accelerating cavities, which use radiofrequency (RF) fields to accelerate the ions. The RF field in an accelerating cavity is given by below equation 2.3:

$$E = E_0 \sin(\omega t + \varphi) \tag{2.3}$$

where E0 is the peak electric field strength, ω is the angular frequency of the RF field, t is time, and φ is the phase of the RF field. The magnetic force on an ion in a magnetic field is given by the Lorentz force law, which states that the magnetic force on a charged particle is equal to the product of the charge of the particle, the magnetic field, and the velocity of the particle. The magnetic field in a LINAC is typically produced by a series of bending magnets, which use static magnetic fields to bend the ion beam. The static magnetic field in a bending magnet is given by:

$$B = B_0 \tag{2.4}$$

where B_0 is the strength of the static magnetic field. The equation of motion for an ion in a LINAC can then be written as:

$$F = ma = q(E + v \text{ x } B) \tag{2.5}$$

where F is the net force, m is the mass of the ion, a is the acceleration, q is the charge of the ion, E is the electric field, v is the velocity of the ion, and B is the magnetic field.

The second equation in the longitudinal beam dynamics is the energy conservation equation, which describes how the energy of the ions changes as they are accelerated through the LINAC. The energy of an ion in a LINAC is given by the sum of its kinetic energy and its potential energy. The kinetic energy of an ion is given by equation 2.6:

$$E_{kin} = {}^{1}/_{2} mv^2 \tag{2.6}$$

where m is the mass of the ion and v is its velocity. The potential energy of an ion in an electric field is given by equation 2.7:

$$E_{pot} = qV \tag{2.7}$$

where q is the charge of the ion and V is the electric potential. The energy conservation equation for an ion in a LINAC can then be written as:

$$\Delta E = \Delta E_{kin} + \Delta E_{pot} = 0 \tag{2.8}$$

where ΔE is the change in energy, ΔE_{kin} is the change in kinetic energy, and ΔE_{pot} is the change in potential energy.

The third equation in the longitudinal beam dynamics is the phase space equation, which describes the distribution of the ions in phase space. Phase space is a mathematical construct used to represent the position and momentum of a particle. The position and momentum of an ion in a LINAC can be described by the coordinates x, px, y, and py, where x and y represent the position of the ion in the beamline and px, py represent the momentum of the ion. The phase space equation for an ion in a LINAC is given by the Liouville equation, which states that the phase space distribution of the ions is conserved as they are accelerated through the LINAC.

The phase space equation is important because it allows us to predict the behaviour of the ions in the beamline as they are accelerated through the LINAC. For example, if we know the initial phase space distribution of the ions, we can use the phase space equation to predict how the ions will be distributed in phase space at any given time. This information is useful in designing and optimizing the LINAC to produce high-energy ion beams with desirable properties.

In addition to the above set of equations, there are a number of other quantities that are used to describe the longitudinal beam dynamics in a LINAC. One such quantity is the energy spread, which is defined as the difference in energy between the highest and lowest energy ions in the beam. The energy spread can be caused by a number of factors, including fluctuations in the accelerating fields, scattering of the ions, and space charge effects. The energy spread can be related to the beam emittance, which is a measure of the beam's phase space distribution. The beam emittance is defined as the product of the beam's transverse size and angle, and is typically expressed in units of mrad. The beam emittance is an important parameter in the design of a LINAC, as it determines the focusing properties of the beam.

However, it is possible to add additional equations to the set of longitudinal beam dynamics equations depending on the specific requirements of the LINAC and the ions being accelerated. For example, if the ion beam is subject to space charge forces (i.e., the Coulomb forces between the ions in the beam), an additional equation known as the Poisson equation can be used to describe the electric potential created by the space charge. Similarly, if the ion beam is subject to wakefields (i.e., fields generated by the passage of the ion beam through a medium), an additional equation known as the Wakefield equation can be used to describe the effect of the wakefields on the ion beam.

2.2 Momentum and Momentum spread in accelerators

From the previous chapter it is known that in an accelerator, charged particles are accelerated to high energies over a distance of several meters by means of electromagnetic fields. The acceleration process imparts kinetic energy to the particles, which is reflected in an increase in their momentum. The momentum of a particle is a measure of its motion and is defined as the product of its mass and velocity. In the case of charged particles in a linac, the momentum is also influenced by the electric and magnetic fields that are used to accelerate them. The momentum of a particle can be described mathematically using the following equation 2.9:

$$p = mv \tag{2.9}$$

where p is the momentum of the particle, m is its mass, and v is its velocity. The relationship between the momentum of a particle and the force acting on it can be described by the following equation 2.10:

$$F = dp/dt \tag{2.10}$$

where F is the force acting on the particle, p is its momentum, and t is time. This equation states that the force acting on a particle is equal to the rate of change of its momentum with respect to time. One way to describe the momentum of the particles in an accelerator is to consider the phase space of the system, which is a six-dimensional space that includes three dimensions of position and three dimensions of momentum. The phase space distribution of the particles reflects the range of momentum values that they possess at a given point in time. In general, the momentum of the particles in an accelerator will spread out over a range of values as they are accelerated. This momentum spread can arise due to a variety of factors, such as the initial energy spread of the particles, the focusing properties of the accelerator, and the presence of perturbations or noise in the acceleration process. The momentum spread of the particles in an accelerator can have significant consequences for the performance of the accelerator and the quality of the particle beam that it produces. For example, a large momentum spread can lead to emittance growth, which is an increase in the size of the beam in phase space and can result in a degradation of beam quality. Emittance growth can be caused by a variety of factors, such as space charge effects, scattering, and imperfections in the accelerator lattice.

To minimize the momentum spread and emittance growth in an accelerator, it is important to carefully design the acceleration process and the accelerator lattice. This can involve using specialized beam-steering and focusing elements, such as quadrupole magnets and skew quadrupole magnets, to control the trajectory of the particles and keep them on a desired path. In addition, it may be necessary to use feedback systems to actively correct for perturbations and noise in the accelerator.

In summary, the momentum of the particles is an important parameter that determines the energy of the particle beam and the performance of the accelerator. The momentum spread of the particles reflects the range of momentum values that they possess and can have significant consequences for the beam quality and emittance growth. Careful design and control of the acceleration process and the accelerator lattice is necessary to minimize the momentum spread and maintain a high-quality beam.

2.3 Harmonic number and Slippage factor

Harmonic number (n): In signal processing, a harmonic is a sinusoidal component of a signal with a frequency that is a multiple of the signal's fundamental frequency. The fundamental frequency is also known as the first harmonic, and the other sinusoidal components are known as higher harmonics. The harmonic numbers of a signal can be used to describe the frequency content of the signal. For example, a signal with a single harmonic would be a pure sine wave, while a signal with multiple harmonics would have a more complex frequency content. In general, the more harmonics a signal has, the more complex its frequency content will be. Harmonics can be either odd or even. Odd harmonics will contain a component of the signal that is out of phase with the fundamental frequency, while even harmonics will be in phase with the fundamental frequency. A common method for analyzing the harmonic content of a signal is the Fourier transform, which can be used to decompose a signal into its individual frequency components. The magnitude and phase of each frequency component can then be used to determine the harmonic content of the signal. In addition to analyzing the harmonic content of a signal, harmonic numbers can also be used to generate new signals with specific frequency content.

Slippage factor: The slippage factor, also known as the phase slip factor denoted by ‘η’, is a measure of the deviation of the phase of the particles in the accelerator from the ideal trajectory. It is defined as the ratio of the phase deviation to the ideal phase advance per turn. In other words, it measures how much the particles deviate from the ideal trajectory as they pass through the accelerator. The slippage factor is caused by several factors, including the effects of imperfections in the accelerator's magnetic and electric fields, the presence of electromagnetic noise, and the interactions between the particles and the accelerator's materials. These factors can cause the particles to deviate from their ideal trajectory, leading to a reduction in the overall performance of the accelerator. The formula for the slippage factor written as:

One of the main effects of the slippage factor in a Linac is that it can cause the particles to lose energy as they pass through the accelerator and that it can cause the particles to spread out in energy. This is because the particles are not following the ideal trajectory, and they are not receiving the full amount of energy from the electromagnetic fields. As a result, the particles will have a lower final energy than they would have if the slippage factor were zero. The slippage factor can also cause the particles to lose synchronism. There are several ways to reduce the slippage factor in particle accelerators. One of the most effective ways is to use high-precision magnetic and electric fields to minimize the effects of imperfections. Another way is to use electromagnetic shielding to reduce the effects of electromagnetic noise. Additionally, the use of special materials, such as superconductors, can also help to reduce the slippage factor.

2.4 Linac to Filter line (ITF) at LINAC3

In this section, the theoretical concepts of the main acting elements of the linac to filter line also known as the ITF line at LINAC3 are discussed starting with the stripper box where the foils with different densities are placed and the stripping of electrons takes place. Then a detailed explanation of Ramping cavity and the Debuncher cavity is discussed. Figure 7 depicts the layout of the filter-stripper line where the particle beam direction is from right to left with an indication arrow on the top. To the far right is the end of LINAC3 tank 3 which then follows the stripper box. Next to the stripper box is the Ramping cavity (RC) indicated in blue colour and after a certain distance to the left, the Debuncher cavity (DC) is placed also in blue colour.

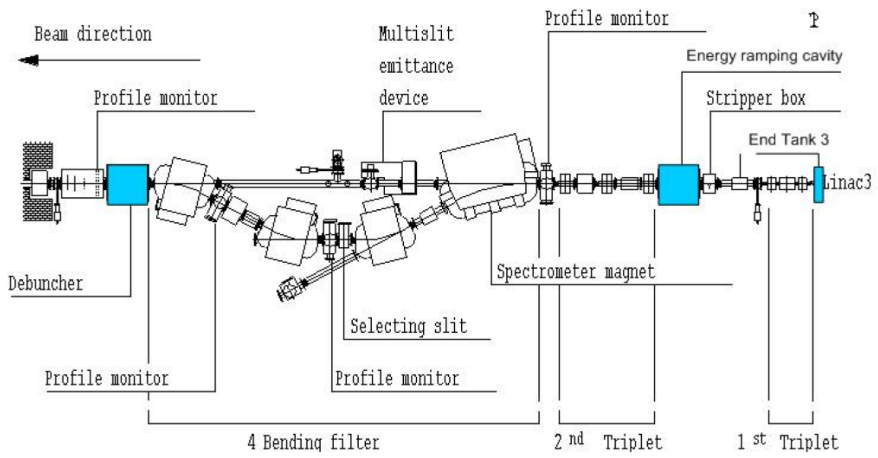

Figure 7: Design layout of the Linac to Filter line.[7]

2.4.1 Stripper Foils

In particle accelerators, stripper foils are thin sheets of material that are used to strip or remove electrons from the surface of a beam of charged particles. This is typically done to increase the energy of the beam by stripping or removing the outer electron shells from atomic nuclei. This process, known as atomic stripping, is used to produce highly charged ions (HCIs), which are ions with a large number of positive charges therefore less magnetic field to blend into the ring is required and allow it to be accelerated to higher energies. Several types of stripper foils are used in particle accelerators, including carbon, aluminium, copper, and diamond foils. In this thesis carbon stripper foils are considered for measurements and analysis.

These carbon foils are typically placed in the path of the particle beam, and as the particles pass through the foil the electrons are stripped from their surface and collected on an electrode located on the other side of the foil. Carbon stripper foils are used in producing HCIs because they have a high atomic number, making them effective at stripping electrons from atomic nuclei. They are typically made of graphite or diamond-like carbon, and are usually several micrometres thick. The thickness and material of the stripper foil are important factors in determining the efficiency of the stripping process. Thinner foils are generally more efficient at stripping electrons, but they also have a higher risk of damaging the beam or the accelerator structure as they can break easily due to the incoming energy of the beam. HCIs are used in a variety of applications, including cancer treatment, material science research, and the study of fundamental nuclear physics.

Below figure 8 depicts the images of the GSI carbon stripper foils installed in the stripper box at LINAC3 with different foil densities of 77, 78, 128 and 128 $\mu g/cm^2$ respectively. It should be understood that the energy of the beam at the foil determines the available charge states for the Ions moving further through the accelerator. The ions passing through the foil lose additional electrons.

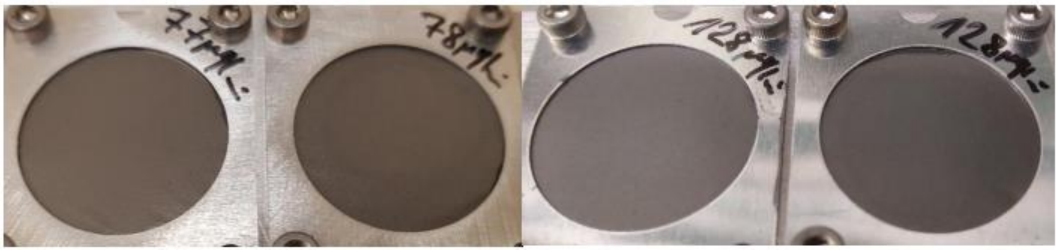

Figure 8: Stripper foils with different thicknesses (77, 78, 128, and 128μg/cm^2)

Here in the case of Lead (Pb) ion, from the source at the beginning of the LINAC3 we get Lead with the charge state of Pb29+ and receive the beam at an energy of 4.2MeV/u. After the Ion beam passes through the stripper box through the carbon foils, we obtain Lead with a charge state of Pb54+ by stripping 25 electrons while having a mean energy loss. Pb54+ is meant to be a right charge state after stripping since in the past Lead ion with a charge state of Pb53+ had an electron capture issue with the electron cooling and Pb55+ is less abundant at 4.2MeV/u. Then this Ion beam with a charge state of Pb54+ traverses further towards the energy Ramping cavity and then to the Debuncher cavity.

2.4.2 Energy Ramping cavity and Debuncher cavity

In a linear accelerator, a ramping cavity [7] is a specialized type of RF (radio frequency) cavity that is used to gradually increase the energy of a beam of charged particles as it passes through the accelerator. The ramping cavity is designed to operate at a frequency that is resonant with the energy of the beam. As the beam passes through the cavity, it absorbs energy from the RF field, which causes its energy to increase. By gradually adjusting the frequency of the RF field in the ramping cavity, the energy of the beam can be increased in a controlled and continuous manner. The ramping cavity is typically used in conjunction with other RF cavities in the linear accelerator, which are used to maintain the energy of the beam and to shape its beam profile. Together, these cavities form a complex RF system that is used to accelerate the beam to the desired energy. The ramping cavity plays a critical role in the operation of a linear accelerator, as it allows for the precise and efficient acceleration of the beam to high energies. It is an important component of many accelerator systems, including those used in high-energy physics research, medical isotope production, and material processing.

For LEIR to accumulate ions over the combined longitudinal-transverse multiturn injection, a variation of linac momentum (ramping) by +/-0.2% with the 200µs of ramping time is required. This variation of the linac momentum is provided by the Ramping cavity (RC). A fast modulation is required to the amplitude or phase of the ramping cavity for ramping and also the phase of the next-in-line cavities had to be modulated to the same technique to indemnify for the change in time of flight. At the end of the ramping, the beam gets an average increase in energy or the momentum spread $\Delta p/p$ but maintains the same energy of the beam at 4.2Mev/u i.e., the energy of the whole beam remains the same at the entry and exit of the cavity. This energy spread was an effect due to modulation reaching the limits and is compensated by choosing a nominal working point that gave the minimal energy spread. With the help of Ramping cavity, the mean energy of the whole beam can be controlled. The ramping cavity is operated in two ways. The first way is phase modulation where the phase is varied symmetrically during the time of ramping around the zero-crossing phase. The second way is by amplitude modulation where the amplitude is varied by placing the beam on the crest of a Radiofrequency (RF) wave. Both the phase and amplitude modulation have the limitation of longitudinal emittance of the beam as the beam can reach the non-linear region of the RF wave from modulation and leading to the increase in energy spread. The Ramping cavity in principle can work at frequencies of 101 MHz and 202 MHz but at 202 MHz the phase width of the beam is doubled having a direct effect on the increase in the energy spread of the beam. Due to this reason, the 101 MHz is treated as the operating frequency of the cavity.

Considering the case of amplitude modulation technique, the modulated signal can be used to control various aspects of the accelerator, such as the intensity of the beam, the position of the beam within the accelerator, or the focus of the beam. It can also be used to transmit information about the state of the accelerator or the particles being accelerated, such as their energy, charge, or mass., Applying the amplitude modulation technique for the Ramping cavity, during the 200 µs of ramping time there should be a voltage sweep from -162 kV to +162 kV. In a detailed explanation, the voltage is brought down from maximum to zero in 100 µs, then 180° phase rotation is applied and the voltage is brought back to the maximum from zero. The main disadvantage of this technique is the difficulty in 180° phase rotation.

The phase of the signal inside a cavity is a measure of the position of the electromagnetic wave at a particular point in time. It is defined as the fraction of a full oscillation that the signal has undergone, and is typically expressed in degrees or radians. The phase of the signal can be affected by various factors, including the size and shape of the cavity, the frequency of the signal, and the presence of any external perturbations. In the case of Phase modulation technique, that can be used to control the phase of the electromagnetic signal inside a cavity in a particle accelerator. It involves adding a small, periodic variation to the phase of the signal, which can be used to alter the characteristics of the cavity or the particles being accelerated. One common application of phase modulation is to stabilize the phase of the signal in the cavity, which is important for maintaining stable operation of the accelerator. When the phase of the modulation signal is properly adjusted, it can cancel out any phase variations in the cavity, resulting in a more stable signal. Phase modulation can also be used to control the beam properties of the particles being accelerated. For example, it can be used to focus the beam or to adjust the energy of the particles. This is often achieved by adding a phase modulation signal with a frequency that is different from the resonant frequency of the cavity. The specific frequency and phase of the modulation signal will depend on the desired beam properties and the characteristics of the cavity. For the Ramping cavity, during the same 200 µs of ramping time, the phase should sweep within a range of ±40°. It is important to choose the phase limits so that the beam stays in the linear region of the RF wave all the time during the ramping process and hence the voltage is higher than in the case of amplitude modulation.

Figure 9(A) shows the single injected pulse from LINAC3 with a pulse length of 200 µs and a slice of the pulse is shaded in blue colour. Figure 9(B) depicts the energy-phase space diagram of that single slice with energy spread at the end of the ramping process in the Ramping cavity.

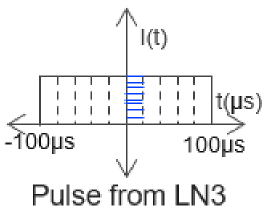

(A)

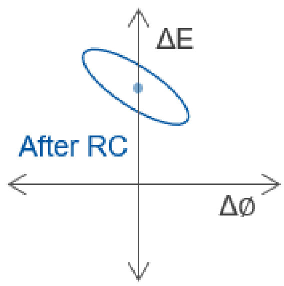

(B)

Figure 9: A shows the single pulse from LINAC3 injected into LEIR. B shows the slice of the beam from 200 µs pulse plotted in energy-phase space diagram after ramping

Next the beam traverses to the Debuncher cavity (DC), the debuncher cavity [7] is a type of radio frequency (RF) cavity that operates in similar fashion compared to the Ramping cavity but the Debuncher cavity is used to bunch and debunch the particle beam as it travels through ITF line of LINAC3. The process of bunching and debunching involves grouping the particles into small packets, or bunches, which are then separated by a specific distance. This allows the particles to be more effectively accelerated and controlled as they pass through the accelerator. When the beam reaches the debuncher cavity there is no change in energy foreseen during the time of flight for the beam within the 12m drift space between the Ramping cavity and the Debuncher cavity (DC) but few particles arrive with a delay and few particles arrive early to the Debuncher cavity as shown in the below Figure 10 (A). At the Debuncher cavity, the delayed particles are accelerated by giving an increase in energy whereas the particles that arrive early are decelerated by giving a decrease in energy. In principle, this is done by phase-space rotation technique as shown in the below Figure 10 (B). With the help of this technique, the ramped energy beam with a reduction in the energy spread is observed at the end of the Debuncher cavity as shown in the below Figure 10 (C).

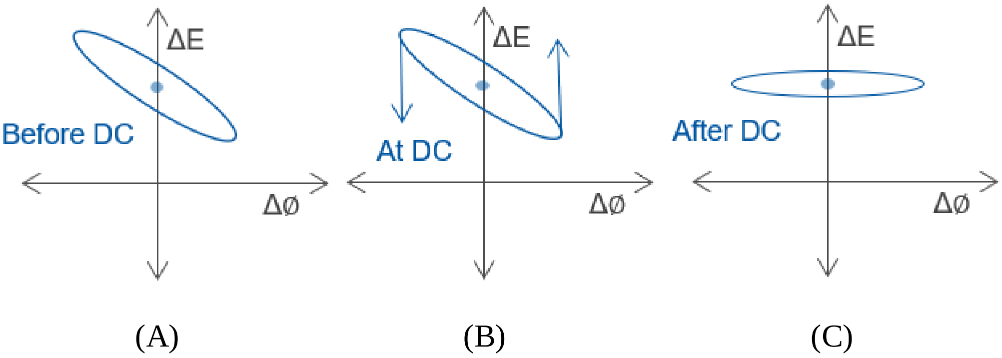

Figure 10: A shows the ramped beam arriving at Debuncher cavity. B shows the phase-space technique applied at the Debuncher cavity (DC). C shows the beam at the output of the DC.

Now let us consider another slice of the pulse in the 200 µs single injected pulse from LINAC3 at a different position in time indicated with black stripes as shown in below Figure 11 (A). The output of the two slices in energy phase-space diagram at the end of the Debuncher cavity is depicted in the below Figure 11 (B). It is observed that there is reduction in energy spread and also the difference in energies.

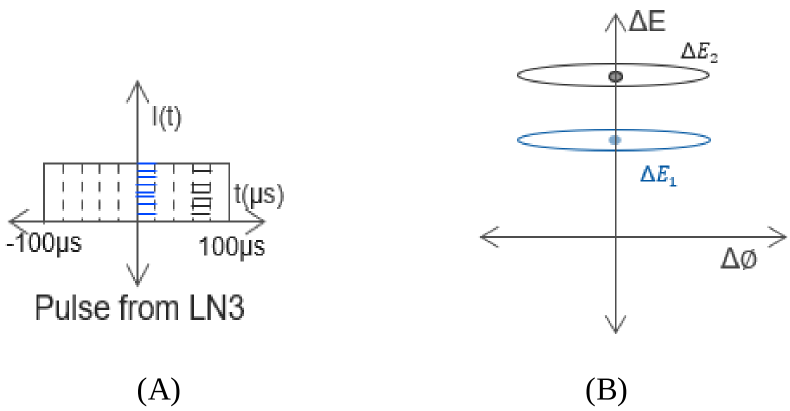

Figure 11: A shows the slice-by-slice single pulse from LINAC3 injected into LEIR. B shows the two slices of the beam at the output of Debuncher cavity.

Chapter – 3

Schottky signals

In this chapter we will get familiar with the theoretical topic about the shot noise, get acquainted with the measurement of Schottky signals [9] and will be having an overview about the Schottky signal monitoring application which is used to view and adjust the properties of the incoming beam into LEIR.

In circular accelerators, when a large number of particles are circulating within the accelerator, exhibits a random component by the beam current called as Shot noise or Schottky noise. Schottky signals are useful to study the accelerator performance whether the beam is bunched or unbunched and traversing in the longitudinal or transverse direction. The LEIR Schottky beam diagnostics system [8] helps us in measuring important beam parameters such as momentum spread, tune, chromaticity, etc., Throughout this chapter, we will be discussing the information regarding the measurement of the signal in longitudinal plane of an unbunched beam.

3.1 Shot noise

Shot noise was first discovered by Walter Schottky in 1918 during his experiments with vacuum tubes. It was observed from the noise resulting from a transition between two charged carriers occurs in a system with shot noise. Shot noise or also known as Schottky noise is a type of noise that arises in electronic systems due to the discrete nature of the electric charge. In other words, it is a type of noise that is caused by the random fluctuations in the number of charge carriers (such as electrons) that pass through a conductor in a given time interval. This type of noise is often observed in electronic devices that involve the transport of charge carriers, such as photodetectors, solar cells, and electronic amplifiers.

One way to understand shot noise is to consider two plates, an anode, and a cathode, in a vacuum environment connected to a DC (direct current) supply as shown in below figure 12. The current is carried by a stream of electrons moving from cathode to anode, which are the charge carriers in this case. The number of electrons that pass-through a given cross-sectional area between the plates in a given time interval is subject to random fluctuations. These fluctuations give rise to shot noise. The amount of shot noise in a system is determined by the number of charge carriers that pass through the system. This means that the noise power is proportional to the square root of the average number of charge carriers per unit of time. Subsequently, the direct current generates a total shot noise Power Spectral density (PSD) given as

$$PSD = 2eI_0 \tag{3.1}$$

where I_0 is the direct current (DC), e is the elementary charge.

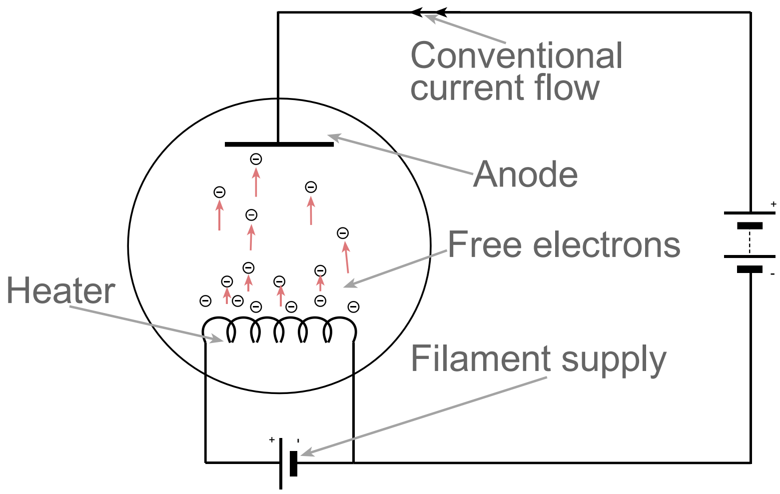

Figure 12: Vacuum diode

Shot noise is typically observed at low current levels, where the fluctuations in the number of charge carriers are more pronounced. At high current levels, the fluctuations tend to average out and the noise is less noticeable.

Schottky Pick-ups: A Schottky pick-up system [10], also known as a Schottky detector, is a device used to detect charged particles in particle accelerators. It is a beam diagnostic monitor typically used to measure the intensity and distribution of particle beams in the accelerator, as well as to monitor the beam position and profile. The basic components of a Schottky pick-up system are a metal strip, or "strip-line," embedded in a dielectric material such as ceramic or glass. The strip-line is typically located near the centre of the detector and is surrounded by a ground plane. When a charged particle passes through the detector, it can knock electrons off of the metal atoms in the strip-line, creating a current in the strip-line. This current is proportional to the number of charged particles passing through the detector. There are several other different types of Schottky pickups that are used in particle accelerators, each with its own unique characteristics and applications. For example, some Schottky pickups are designed to be mounted on a beam pipe and are used to detect charged particles in the beam as it passes through the accelerator. Others are designed to be mounted on a support structure and are used to measure the intensity and distribution of the beam as it exits the accelerator. The two main types of Schottky pick-up systems are the short strip-line pick-ups and travelling wave pick-ups.

Short strip-line Schottky pickups detect charged particles in particle accelerators. They are typically used to measure the intensity of the charged particle beam and their distribution in the accelerator, as well as to monitor the beam position and profile. One key feature of short strip-line Schottky pickups is their fast response time, on the order of a few nanoseconds, making them well-suited for use in high-energy particle accelerators. Additionally, they have a relatively low noise level, making them useful for detecting low-intensity particle beams.

On the other hand, travelling wave Schottky pickups, also known as travelling wave detectors or TWDs, measure the electromagnetic waves that are generated as the low velocity particles pass through the detector. They are similar to short strip-line Schottky pickups, but instead of detecting the charged particles directly, they measure the electromagnetic waves that are generated as the particles pass through the detector. One key advantage of TWDs is their high sensitivity. They can detect very low-intensity particle beams, also have a relatively fast response time typically in order of a few nanoseconds.

In both cases, a preamplifier circuit is used to amplify the small current produced by the detector and then it is sent to a signal processing unit, which converts the current into a voltage signal. This signal can then be further processed to extract information about the beam, such as its intensity, distribution, and position. One important consideration when using Schottky pick-up systems is the choice of metal for the strip-line. Different metals have different electrical conductivity and work function values, which can affect the sensitivity and response time of the detector. For example, gold and platinum are commonly used in Schottky detectors due to their high conductivity and low work function values. In addition to their use in particle accelerators, Schottky detectors are also used in other applications such as X-ray imaging, particle physics experiments, and radiation detection. A cascade of stripline pickups Schottky system [10] is used to study the LEIR machine performance at the injection where the velocity of the particle is low and also due to the generation of the above-discussed random fluctuations. This Schottky system can be enhanced for examining the longitudinal or transverse particle dynamics based on whether the beam is bunched or unbunched.

3.2 Schottky signals for Unbunched beam in the longitudinal plane

Firstly, let us consider a single particle circulating in the machine with charge ‘e’, with revolution frequency f_r, the beam current [13] at a given location in the ring is composed of an infinite train of delta pulses k, with separation of nominal revolution period T_r between each delta pulse as shown in below equation 3.2 and from figure 13.

$$s(t) = \frac{e}{T_r} \sum_{k=-\infty}^{\infty} \delta(t - kT_r) = ef_r \sum_{k=-\infty}^{\infty} \delta(t - kT_r) \quad (3.2)$$

The term ef_r is the Direct current (DC) component that determines the number of times the particle passes over the pick-up system [10] in a second $s_0 = ef_r$. In the below figure 14(A), the periodic waveform can be seen in terms of a line spectrum in frequency domain with the distance between the discrete lines as f_r separated at discrete harmonic numbers n_h.

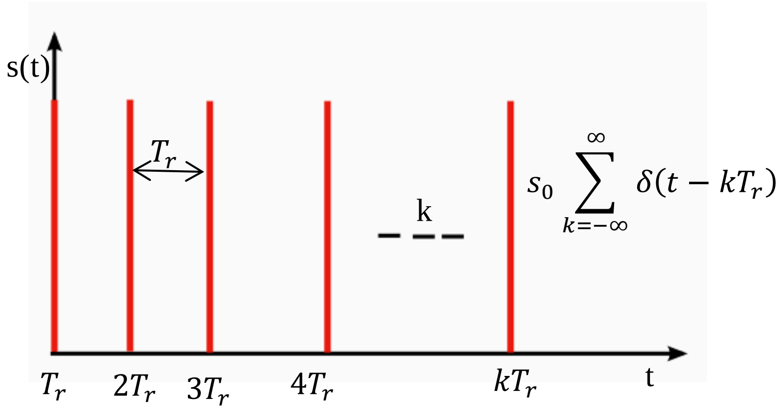

Figure 13: Single particle at a time period of T_r circulating the accelerator

Applying the Fourier transform to the train of delta pulses and rewriting the above equation 3.2 gives equation 3.3

$$s_i(t) = s_0 \sum_{n_h=-\infty}^{\infty} \exp(jn_h 2\pi f_r t) \quad (3.3)$$

Rewriting the above equation 3.3 by taking only the positive frequencies and converting the equation to single-sided spectrum as shown in figure 3.3(A), gives the following equation 3.4 that represents the line spectrum of a particle circulating in an accelerator with frequency f_i.

$$s_i(t) = s_0 + 2s_0 \sum_{n_h=1}^{\infty} \cos(n_h 2\pi f_i t) \quad (3.4)$$

Now let us consider a second particle circulating the accelerator, at slightly different revolution frequency f_1 than the first particle frequency. The below figure 14(B) shows the line spectrum when a second particle represented in blue colour is added, with Δf being the difference between the second and first particle frequency at the harmonic number n_h = 1. The revolution frequency of the second particle [13] is given as:

$$f_1 = n_h \,.\, (f_0 + \Delta f) = n_h f_0 + n_h f_0 \,.\, \eta \frac{\Delta p}{p} \quad (3.5)$$

From the above equation f_0 is represented as the synchronous particle [13] circulating the accelerator at revolution frequency f_r and f_1 is the particle with slightly different frequency resulting due to the relative momentum spread which depends on the slippage factor η of the machine. This in result gives another spectrum line in frequency domain separated from the synchronous particle with an offset of Δf multiplied by the harmonic number n_h.

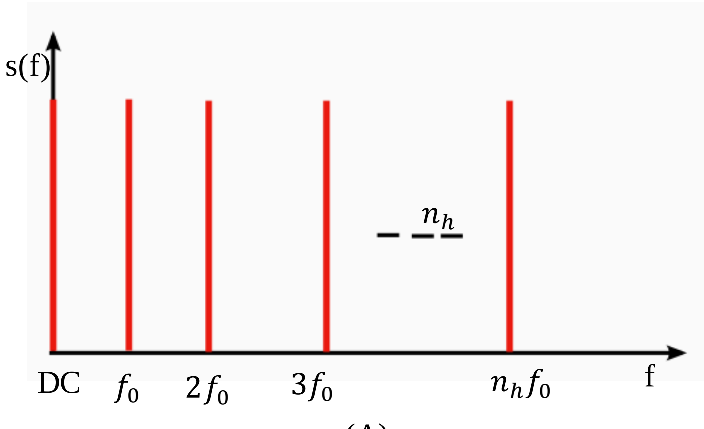

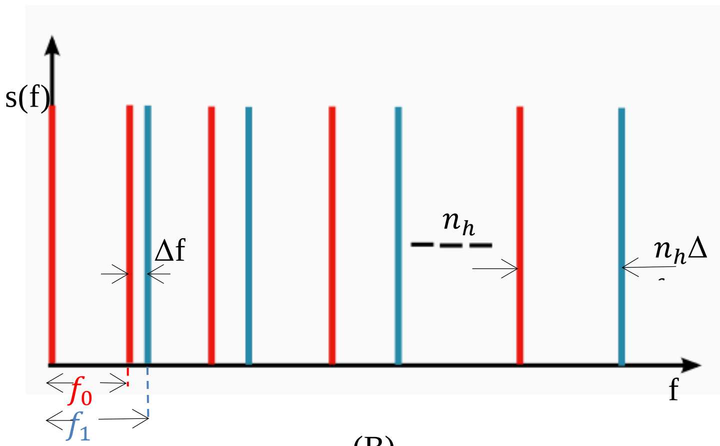

Figure 14: A shows the single particle circulating the accelerator in frequency domain. In B there is an additional particle with a relative momentum spread, which causes it to have a different revolution frequency.

Now let's assume that there are N number of particles added to the unbunched beam that are circulating in the machine, each particle having a distinct revolution frequency. This leads to an infinite narrow pulse width in frequency domain spectrum. These N particles will now replace the separate discrete spectrum lines with a band of frequencies known as the Schottky band as shown in figure 15. The width of each band is determined as $n_h\Delta$f as seen in the above equation 3.5, except the f_0 now denotes the average revolution frequency. Here both f_0 and f_r represents the same, but f_0 is the average frequency of the band and the synchronous particle, whereas f_r is the ideal particle.

Below figure 15 depicts that the width of Schottky band increases and height of the spectral density decreases as a function of harmonic number. As the harmonic number of the frequency continues to increase, at a certain harmonic number the Schottky band [8] overlaps with the previous band (indicated with blue arrow) due to the increase in frequency spread of the sideband and preserving the same band area.

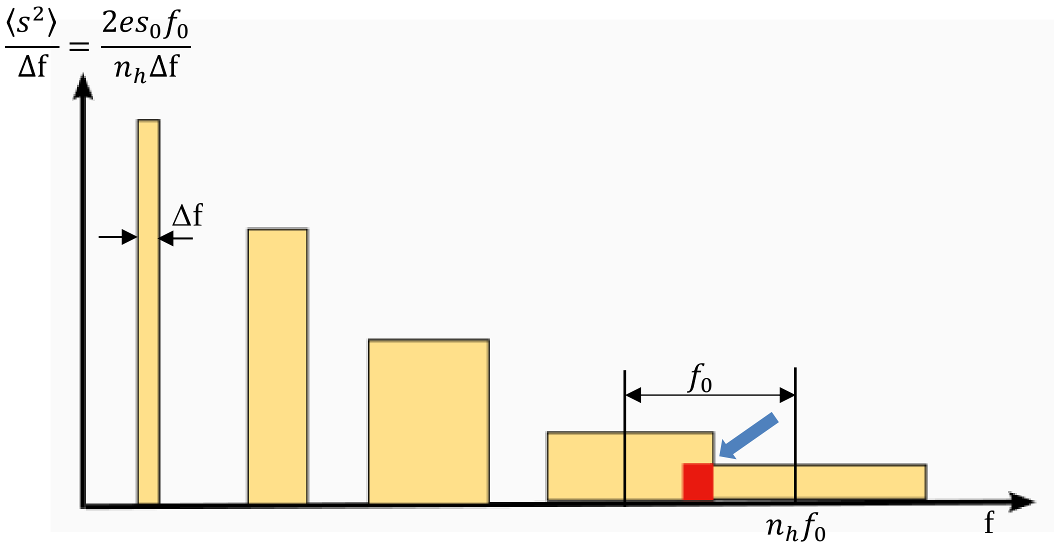

Figure 15: Power spectral density or Schottky bands of the longitudinal Schottky signal, the height of the spectral density reduces as the harmonic number n increases, which causes the width of the band to increase.

The next step is to average equation 3.4 for N particles with different frequencies f_i is given as

$$\langle s_i^2 \rangle = \langle (2ef_0)[\sum_N \cos(n_h 2\pi f_i t)]^2 \rangle = (2ef_r)^2 \sum_N \langle cos^2(n_h 2\pi f_i t) \rangle = 2ef_r^2 N \quad (3.6)$$

3.3 Longitudinal plane Schottky monitor application in LEIR

In order to view, understand and perform measurements with the Schottky signals described in section 3.2 using a Schottky pick-up system, a specialized monitoring tool is required for LEIR. Below figure 16 depicts the Longitudinal plane Schottky monitor application for the LEIR Early cycle, displaying the spectrum signal in the frequency domain. The spectrogram plot on the left side shows the acquisition of beam signal from single injected between 10 to 20 milli-second and it can be seen that the signal is centered at the revolution frequency of the LEIR machine i.e., at 360.5 kHz at second harmonic. The right plot shows the FFT processed power spectral density signal for the very first slice of the spectrogram plot at 10 milli-seconds. On the left part of the image different application settings are shown:

- **FFT length & Number of FFTs:** FFT length is used to control the resolution of the resulting spectra and the number of FFTs determines the size of an FFT i.e., the number of bins to be used for dividing the FFT window into equal bins.
- **Central harmonic:** Used to vary the harmonic number in the interest of the user for viewing the spectra at a particular harmonic.
- **LN3 Ramp Cavity:** Here the start and end phases of the cavity can be varied and optimized to study the machine's behaviour as described in sub-section 2.4.2.
- **LN3 Debunch Cavity:** The start and end phases of the cavity is set to compensate the energy spread resulting from the ramping cavity as described in sub-section 2.4.2.

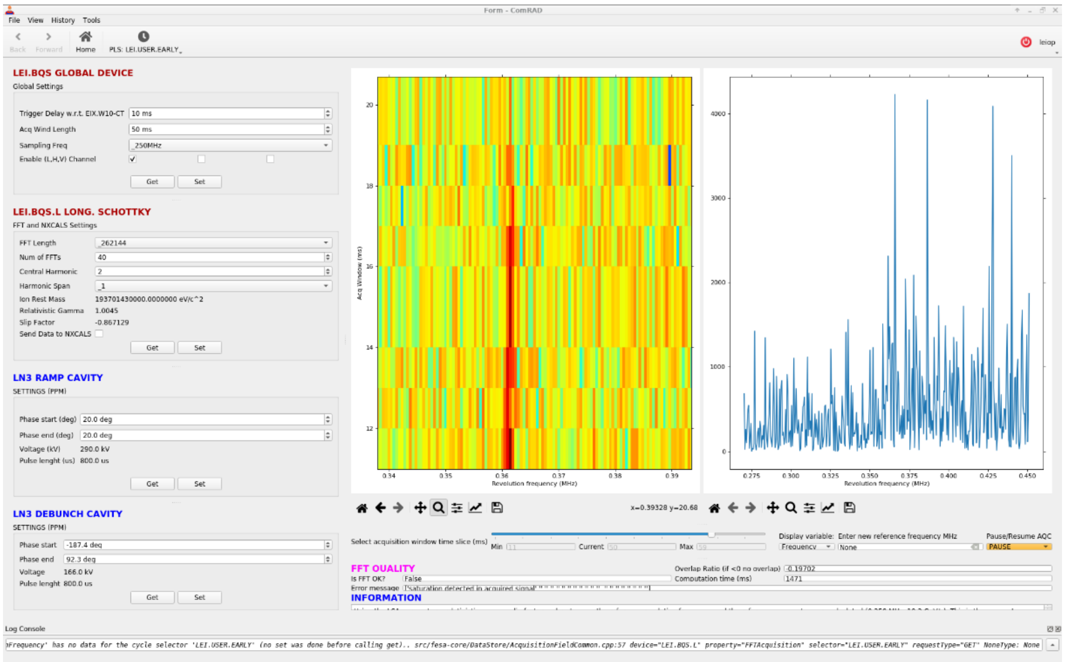

Figure 16: Longitudinal Schottky signal for unbunched beam at 2^{nd} harmonic.

The application also helps to control the other parameters such as enabling or disabling the longitudinal plane channel and transverse plane (horizontal, and vertical channels) for measurements and also other details such as the Ion rest mass, Relativistic gamma ($\gamma = 1.0045$), Slippage factor ($\eta = -0.8671$) of the LEIR machine and the voltage of the Ramping cavity and the Debuncher cavity are shown. Besides the above parameters, it is also possible to change the view, by selecting from the display variable options, the x-axis for the FFT processed power spectral density from the frequency domain to the momentum spread ($\Delta p/p$) domain using the equation 3.5. Figure 17 (A), (B) depicts the spectrogram and power spectral density plot of the Longitudinal plane Schottky signal for the very first slices of the injected beam at harmonic numbers 50 and 100 respectively. It is observed from the below plots that the width of the band increase towards higher harmonics as discussed in above section 3.2 and seen from figure 15. Moreover, the spectrogram is normalized by their respective revolution harmonic in order to stay in the same frequency range and have better sampling.

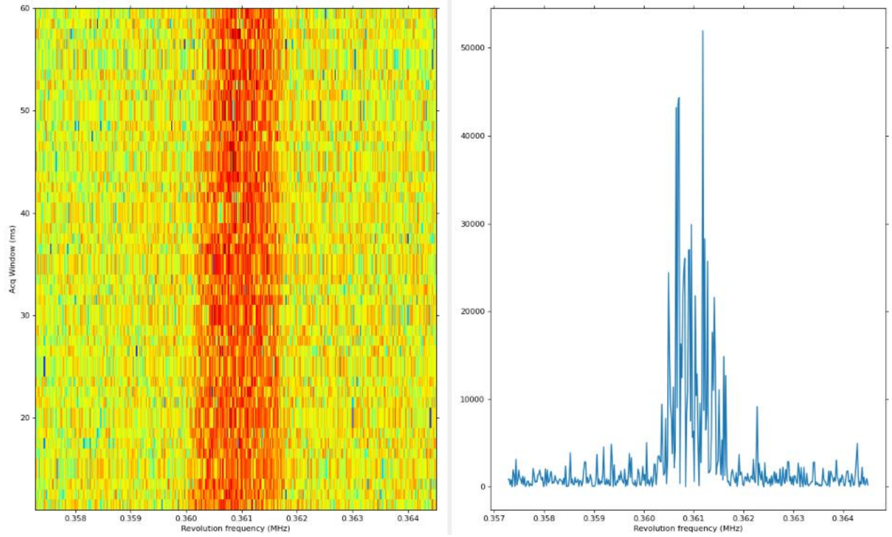

(A)

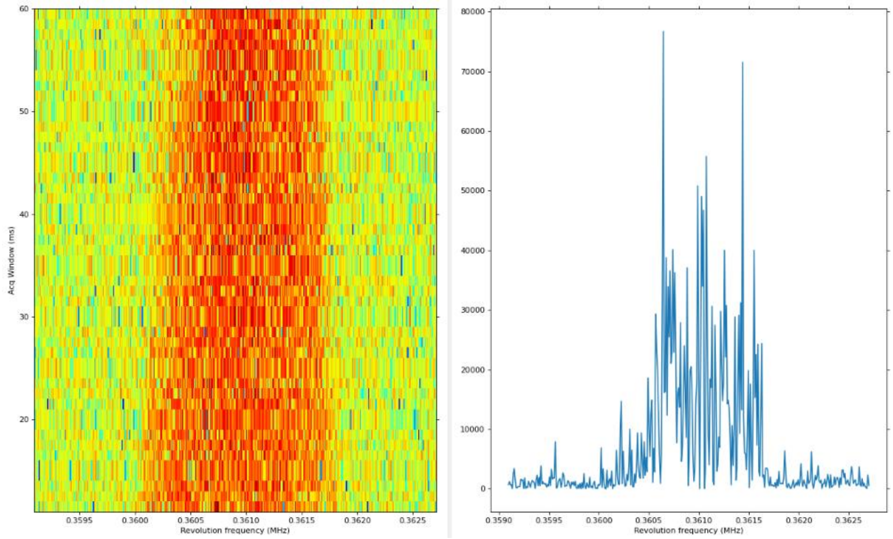

(B)

Figure 17: A shows the Longitudinal Schottky signal for unbunched beam at 50th harmonic and B shows the Longitudinal Schottky signal for unbunched beam at 100th harmonic.

Chapter – 4

Results

In this chapter we will be discussing about the measurement results obtained from the three stripper foils with densities of 97 $\mu g/cm^2$, 127 $\mu g/cm^2$ & 129 $\mu g/cm^2$ upon setting the Ramping cavity phases to their operational phases of 0°, 20°& 40° respectively and performing the static Debuncher cavity phase scan from -70° to 30° with a step width of 10°. The energy scans are performed in static manner by first setting the start and end phase of the Ramping cavity to a particular flat phase, in the same manner setting the debuncher cavity to a constant phase of -70° and the measurements are taken. Next, the Debuncher cavity phase is set to another sequential phase value with a step width of 5° and the measurements are performed again until the phase value reaches 30°. The following measurements are carried out through a series of dedicated joint MD (Machine development) sessions performed between LINAC3 and LEIR. These measurements are done on the EARLY cycle with a single injection pulse from LINAC3, with the electron cooler turned off and with corrected orbit in the machine in order to have a stable beam for measurements. An analysis of two different foils with foil densities of 129 $\mu g/cm^2$ and 127 $\mu g/cm^2$ is explained in order to understand the degradation of the aging foil. The measurement results are benchmarked with the simulation results to predict the behaviour of the energy distribution of the beam coming into LEIR. Also, the development of online monitoring tool for automatized energy scan measurements is presented which helps to characterize the stripper foil behaviour.

4.1 Energy distribution measurements for different Foil densities

Below figure 18 depicts the energy distribution plot for a foil with a density of *129* $\mu g/cm^2$ with Δp/p on the x-axis and arbitrary units on the y-axis. Generally, the measurements are carried out in frequency domain where the x-axis of the plots represents the energy distribution at the particles revolution frequency but to characterize the behaviour of the incoming beam based on the change in momentum spread, the energy distribution is transformed to the Δp/p. This change of the x-axis from the frequency representation to the Δp/p is performed by applying equation 3.5 as stated in section 3.2. The below plot is obtained by performing a Debuncher cavity scan between the phases of -70° to 30° in a static way i.e., by placing the cavity start and end phase to a flat phase single value with a step width of 10° and setting the Ramping cavity start and end phases to the operational flat phase 40°.

The energy scan is performed and the non-gaussian distribution of the beam with the energy spread at that particular Debuncher cavity phases is obtained. Then, the debuncher cavity phase is set to a new flat phase value and the measurements are repeated thus obtaining other distributions of the beam in a similar manner. Each skew-gaussian distribution in below figure 18 represents the particular energy spread of the beam at their respective DC phase. Here the DC phases between -50° to 20° w.r.t the energy spread of the beam are considered for analysis and plotted. It is observed from the plot that when the beam passes through the given stripper foil and by changing the phases of the Debuncher cavity, the energy spread of the beam changes phase by phase. This results in larger width of energy spread at the far end phases of the Debuncher cavity which observed form the below skew-gaussian distributions at -50° and 20°. In contrast the width of energy distribution at Debuncher cavity phase of -20° is narrow. This phenomenon of the change in energy spread occurs due to the fact that when the phase is set to a cavity design limitation value, the beam entering the cavity starts to probe the non-linear part of RF wave, develop high and low energy tails at the particular cavity end phases (DC phase of -50° & 20°) which results in increasing the width towards the energy spread of the beam. It is also understood from the below plot that the peak of each skew-gaussian distribution and its corresponding average energy varies by changing the Debuncher cavity phases due to the phase change seen by the incoming beam at the Debuncher cavity. The main aim of the measurement plot is to understand the behaviour of the energy spread of a beam entering the stripper foil w.r.t the change in DC phases.

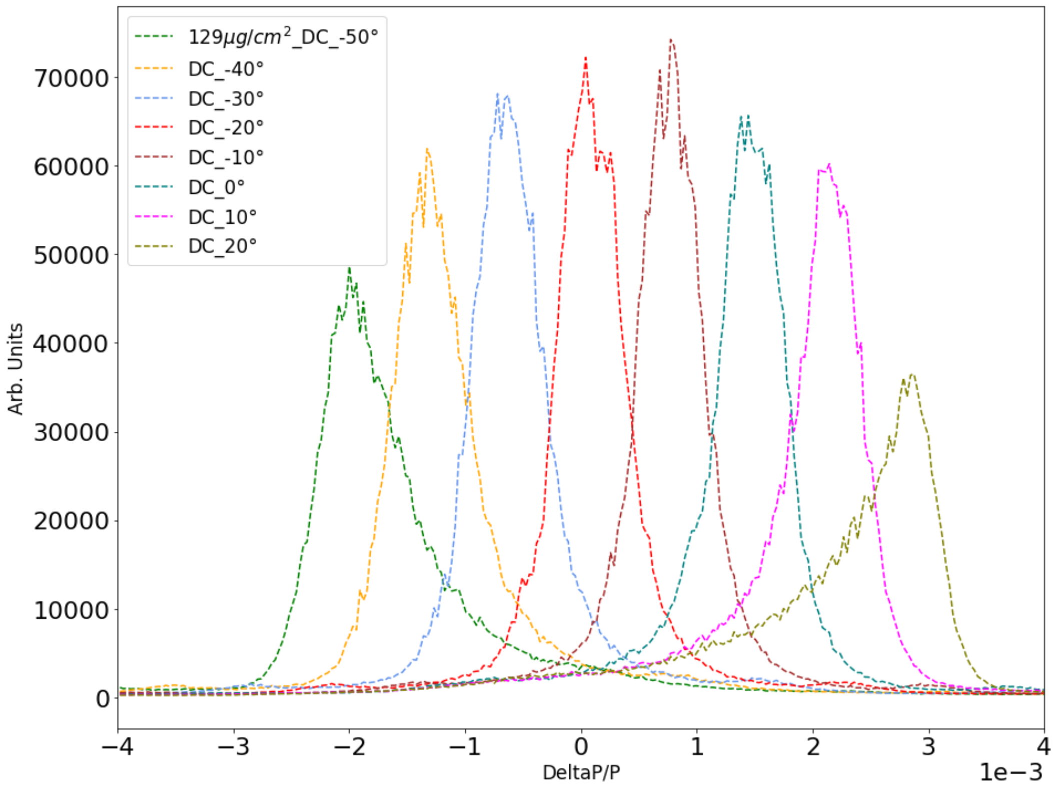

Figure 18: Energy distribution of the beam passing through the 129 μg/cm^2 foil

Following the same procedure stated above, now we replace the existing foil of 129 $\mu g/cm^2$ density to new foils with densities of 127 $\mu g/cm^2$ & 97 $\mu g/cm^2$ and changing the Ramping cavity phases to their operational phases of 20° and 0° respectively. Similar to above measurements, the debuncher cavity phase is set to a constant phase value and the resulting energy spread depicted by the skew gaussian distributions w.r.t DC phases are obtained as shown in below 18 and figure 19. Then, the consecutive flat phase values with a step width of 0° are set at debuncher cavity and the measurements are repeated thus obtaining other gaussian distributions of the beam in a similar manner. Each skew-gaussian distribution from the below plots represents the particular energy spread of the beam at their respective DC phase. Here again the DC phases between -50° to 20° w.r.t the energy spread of the beam are considered for analysis and plotted. It is noticed from the below plots that the width in energy spread of the beam changes phase by phase of the debuncher cavity upon varying the densities of the stripper foils. It is also observed from the below plots that the energy peaks of the skew-gaussian distribution and its corresponding average energies vary w.r.t the change in Debuncher cavity phases. Also, it is difficult to characterize the incoming beam energy spread and understand the behaviour of the stripper foil from one another by looking at figure 18, figure 19 & figure 20 separately. Next, the 3 plots are superimposed upon each other for a better understanding and characterization of the stripper foils with different densities.

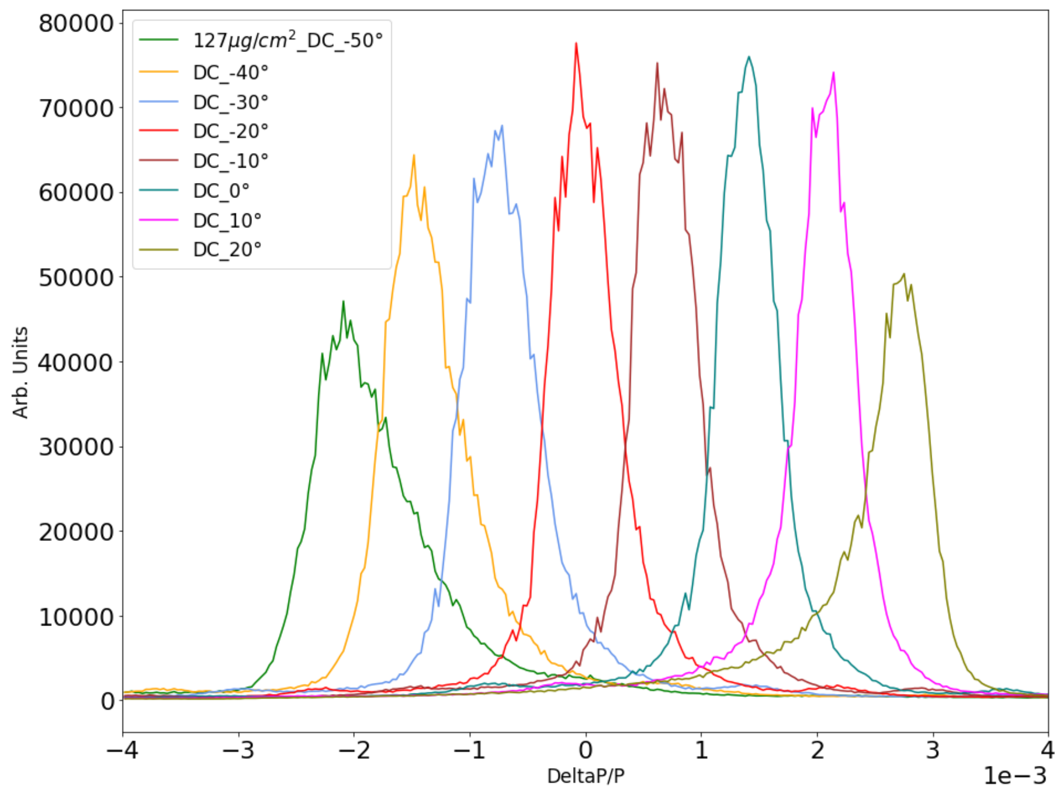

Figure 19: Energy distribution of the beam passing through the 127 μg/cm² foil

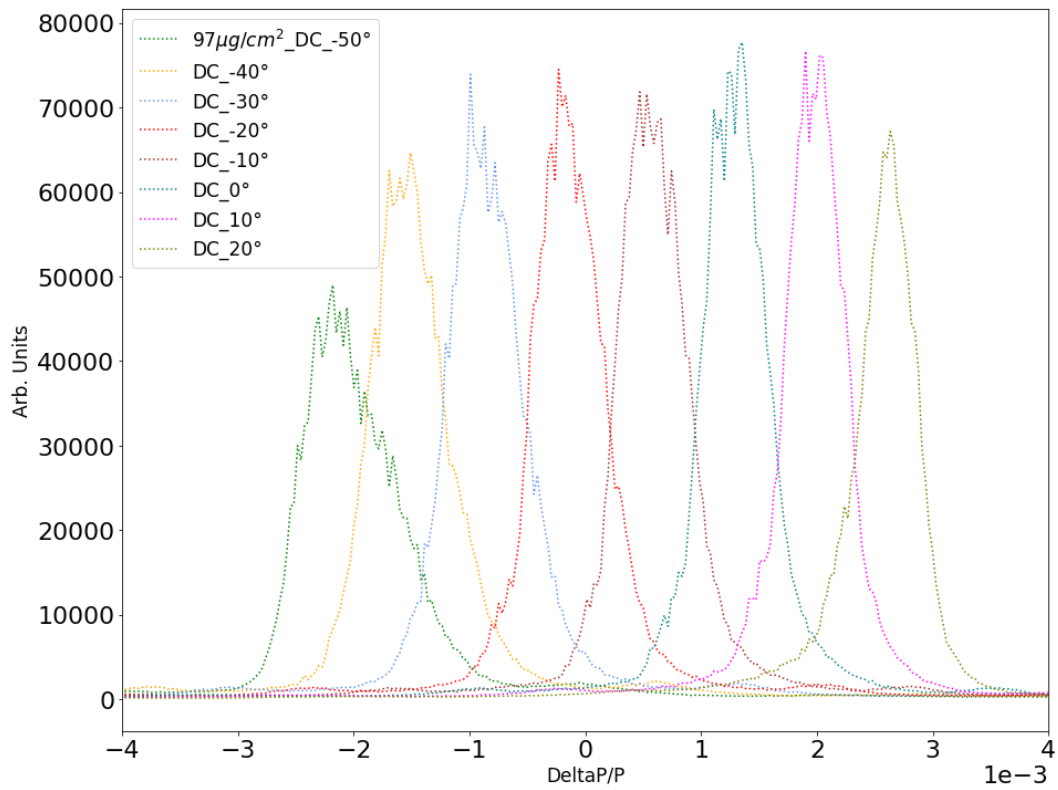

Figure 20: Energy distribution of the beam passing through the 97 μg/cm^2 foil

The behaviour of the stripper foils with different densities through the energy distribution plots can be understood clearly upon viewing the plots in a combined format. So, as of the next step the above three plots are super-imposed upon each other to study the shift in energy distribution and to understand the change in width of the energy spread. In the below figure 21, each energy distribution from the foils with densities of 129 $\mu g/cm^2$, 127 $\mu g/cm^2$ & 97 $\mu g/cm^2$ are plotted w.r.t the Debuncher cavity phases and at their operational Ramping cavity phases of 40°, 20°, 0° respectively. It is also observed that there is a variable change in the width of the gaussian distributions as the density of the stripper foil changes and also it is seen that there is the development of high and low energy tails at the operational limits of the Debuncher cavity phases -50° & 20° respectively for each stripper foil. The main theoretical reason behind the development of the low energy tails at the higher phases of the Debuncher cavity is due to the phase shift inside the cavity from linear regime to the nonlinear regime reaching the crest of a sinusoidal wave. Moreover, it is noticed that the average energy of the Skew-gaussian distributions shifts w.r.t the variation of Debuncher cavity phases and also w.r.t the change in stripper foils densities. It is clearer to understand the behaviour of the skew-gaussian distribution resulting from the energy spread of the beam for each individual stripper foil by having an enlarged view at a particular Debuncher cavity phase and most likely the central phase.

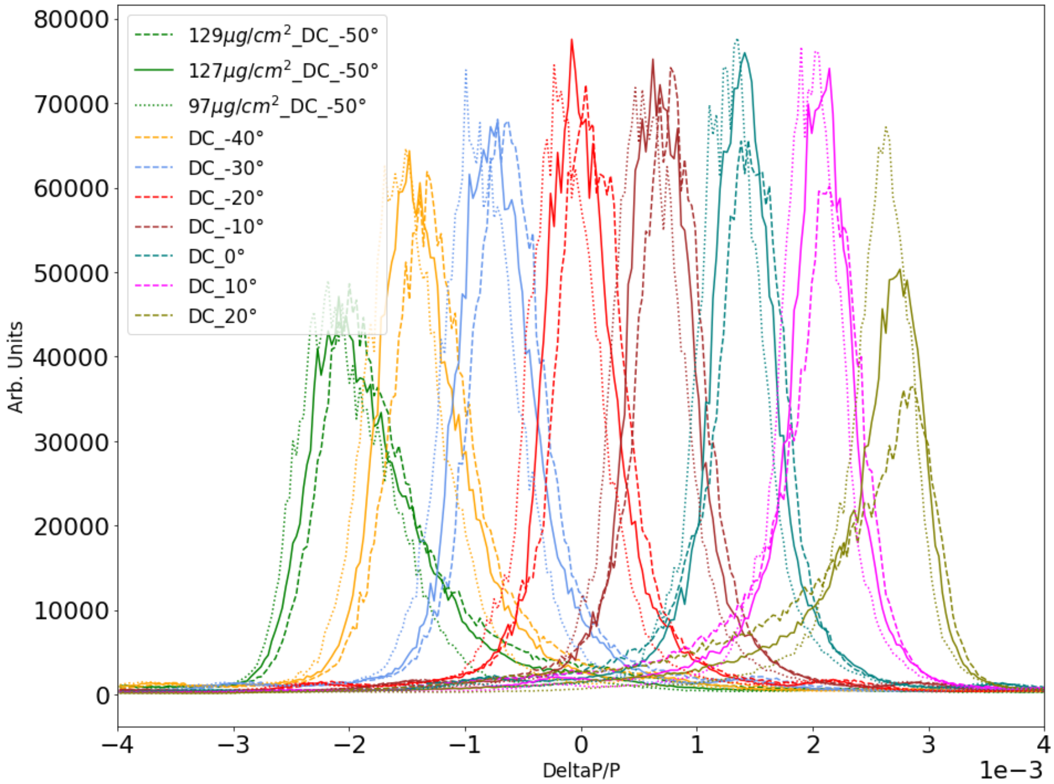

Figure 21: Energy distribution of the beam passing through the 129 μg/cm^2, 127 μg/cm^2 & 97 μg/cm^2 foils

In order to have a clearer view on the behaviour of the stripper foils with different densities, the energy spreads of different stripper foils w.r.t the Debuncher cavity phase of -20° and Ramping cavity phase of 20° is taken for consideration and plotted. The below figure 22 depicts the plot with the central Debuncher cavity phase of -20° and Ramping cavity phase of 20°. The shift in energy distribution can be seen clearly with precision and also gives us the information about the shift in Δp/p as the foil gets thicker and thicker. It is understood clearly now that when a new foil that is thicker than the old one is inserted and the energy scans are performed, a left shift along the x-axis of Δp/p is observed that determines the loss in momentum for heavier foils. This phenomena in the shift occurred mainly due to the variations in the thickness of the stripper foil i.e., the incoming beam experiences the thickness of the foil and causing the Δp/p shift. Another important observation is that there is not only the beam energy varies w.r.t to the change in Debuncher cavity phases but by looking at a particular Debuncher cavity phase it is observed that there is a uniform shift in the energy of the Skew-gaussian distribution when the thickness of the foil changes. The shift observed with the measurements is in good agreement with the theoretical concepts of stripper foils.

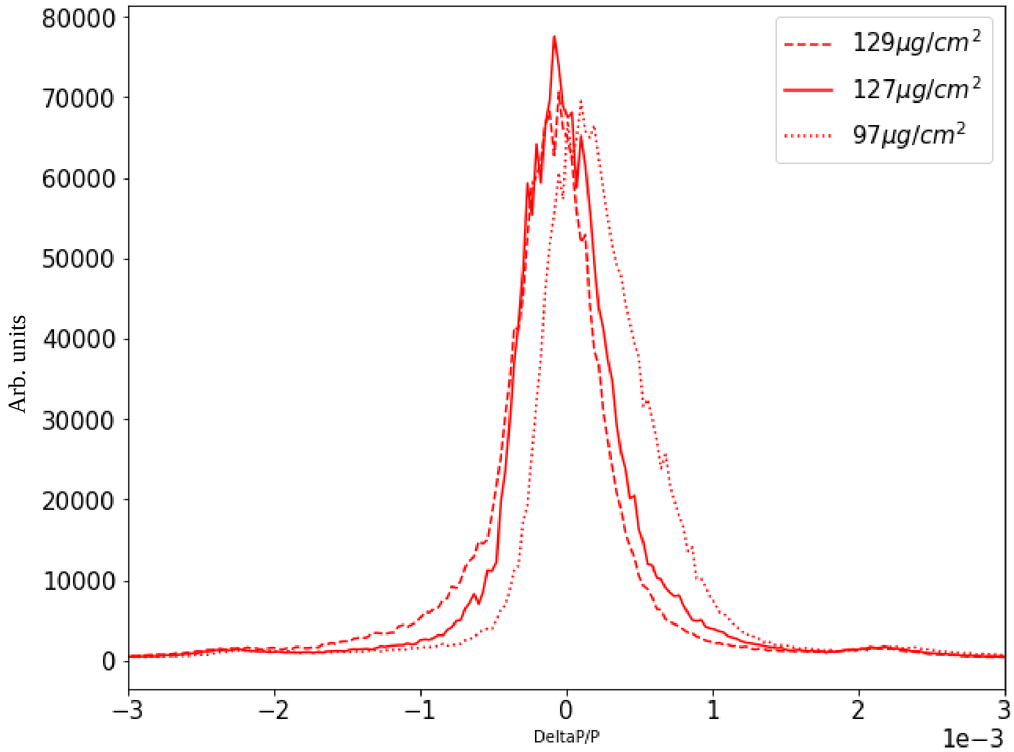

Figure 22: Energy distribution of the beam passing through the 129 µg/cm^2, 127 µg/cm^2 & 97 µg/cm^2 foils viewed at DC phase of -20° and RC phase of 20°

The energy distribution measurements on 127 $\mu g/cm^2$ foil at the Ramping cavity phase of 0° is taken and compared with the simulations [14]. From the below figure 23 the dotted points in different colours represent the measurements taken at different DC phases whereas the dashed line represents the simulated energy distribution results at their respective DC phases. The approach chose to perform the simulations is described as, firstly in LINAC3 before the stripper foil, a simple initial gaussian distribution in energy and phase space regime is taken, then the energy loss due to the stripper foil which is basically the mean shift in energy is simulated with the help of a programming code [15]. Then the beam passage through the Ramping cavity and passage through the Debuncher cavity along with the time of flight between the two cavities is simulated. Next, the output energy distribution of the simulated pulse for each setting with operational phases of ramping cavity and varying static phases of the Debuncher cavity is taken and compared with the measurement results from Schottky system in LEIR. From above discussed measurement results we know that from Schottky diagnosis of a beam we measure the power density spectrum of the beam's revolution frequencies that is normalized back to momentum. Then the simulation code generates the automatic momentum distribution of simulation results and are super imposed with the measurement results (obtained using Schottky diagnostic system in LEIR). It should be noted that in the simulation code the passage of the beam is made synchronous with the sinusoidal wave because in principle the Ramping cavity and the debuncher cavity are following a sine wave working in a linear regime of the cavities. In this regard, it is observed from the below figure 23 by looking at the grey and pink curves that there are the large low energy tails at the higher phases of the Debuncher cavity (mainly at 10° & 20°) because the beam is approaching the crest of the sine wave inside the cavity which is falling under the nonlinear regime and resulting in distortion of the shape of the input gaussian distribution from the simulation. Through this comparison between the measurement and simulated results it is able to predict the energy distribution coming into LEIR accurately and thus benchmarking the results.

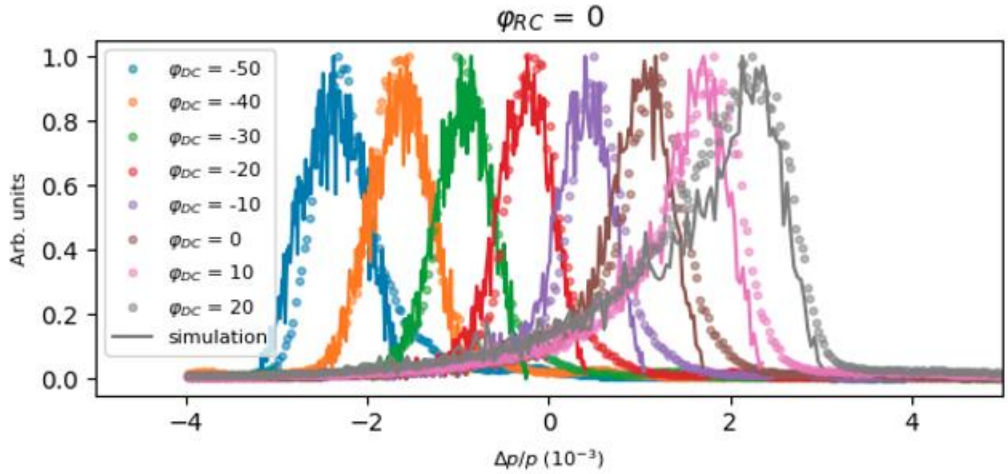

Figure 23: Energy distribution comparison between Measurements vs Simulations for 127 μg/cm² foil at RC phase of 0°

4.2 Analysis of the aging foils with 129 $\mu g/cm^2$ & 127 $\mu g/cm^2$ foil density

Using the measurement results performed on different stripper foils which is used to characterize the energy spread of the incoming beam as discussed in section 4.1, an innovative approach that has been never followed in the past is considered in order to analyze the degradation of the stripper foil and has been presented in this section where a detailed analysis on two foils of 129 $\mu g/cm^2$ & 127 $\mu g/cm^2$ is made to determine the aging or the degradation of the foils over a span of three weeks until the day the foils are broken. The approached method is to consider a stripper foil with a specific density that has been placed in the stripper box that performs stripping mechanism, then it is required to perform the energy scans daily by placing the ramping cavity to its operational phase and varying the debuncher cavity phases in static manner but within the limits of cavity's linear operational regime of phase range (between -50° to 20°). Then the energy measurements are performed over several days and plotted with superimposition, the statistical mean and sigma from the resulting skew-gaussian distribution that determines the change in energy peak and change in width of the distribution respectively is analyzed phase by phase w.r.t the Debuncher cavity. From this analysis it is possible to study any given stripper foil and also to determine the threshold from the sigma plot which will be explained later in this section along with suitable graphs that helps in ascertaining the degradation of the stripper foil well in advance before it is already broken.

Firstly, the foil with the density of 129 $\mu g/cm^2$ is considered for analysis and the energy measurements are made daily from day 5 of the foil installation till day 21 where the stripper foil is broken. Below figure 24 depicts the day-by-day superimposed measurement results obtained for 129 $\mu g/cm^2$ foil at flat Ramping cavity phase of 20° and flat Debuncher cavity phase of 0°. The Debuncher cavity phase of 0° is considered here for a clear view of the energy distribution upon compared with the other Debuncher cavity phases. It is observed from the plot that day-by-day there is an increase in the width of the energy distribution along with a significant shift in energy peak of the skew-gaussian distribution. Moreover, we could see that over time there is a significant left shift in Δp/p and also the development of low energy tails. The reason behind the aforementioned observations is explained below by performing further analysis.

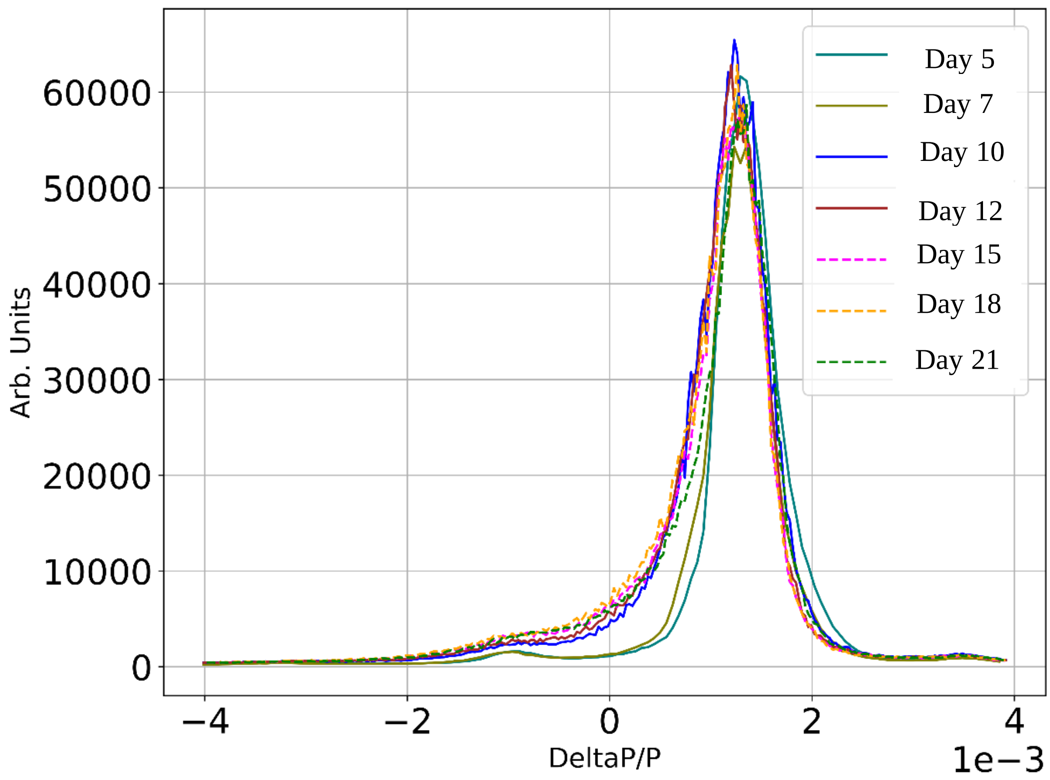

Figure 24: Measurements on 129 µg/cm^2 foil at RC phase of 20° and DC phase of 0°

By looking at figure 24, even though with the increase in the width of the energy spread, development of low energy tails and shift in the Δp/p over time, it is not possible to fully determine the aging of a stripper foil and also the threshold value for a stripper foil at which it is degraded. So, the next step in the analysis of the 129 $\mu g/cm^2$ stripper foil is to calculate and plot the statistical mean and sigma for each individual energy distribution w.r.t the Debuncher cavity phases that are considered form the above-mentioned energy scan measurements. The skew-gaussian energy distributions are taken for each static Debuncher cavity phases between -50° to 20° with a step width of 10° for all the days listed in above figure 24. Their statistical mean and sigma are calculated and plotted which can be seen from the below figure 25 and figure 26 respectively. From the calculation of statistical mean, it is able to analyze the shift in the energy peak of every individual skew-gaussian distribution over time w.r.t each debuncher cavity phases. The below figure 25 depicts the statistical mean plot with the DC phases on x-axis and mean Δp/p on y-axis. The statistical mean towards the higher DC phases mainly from -10° tend to deviate towards a lower mean Δp/p value which is most significant at DC phases between 0° and 20°. The main reason for the deviation towards a lower value over time is due to the aging of the stripper foil which is well observed at the higher Debuncher cavity phases.

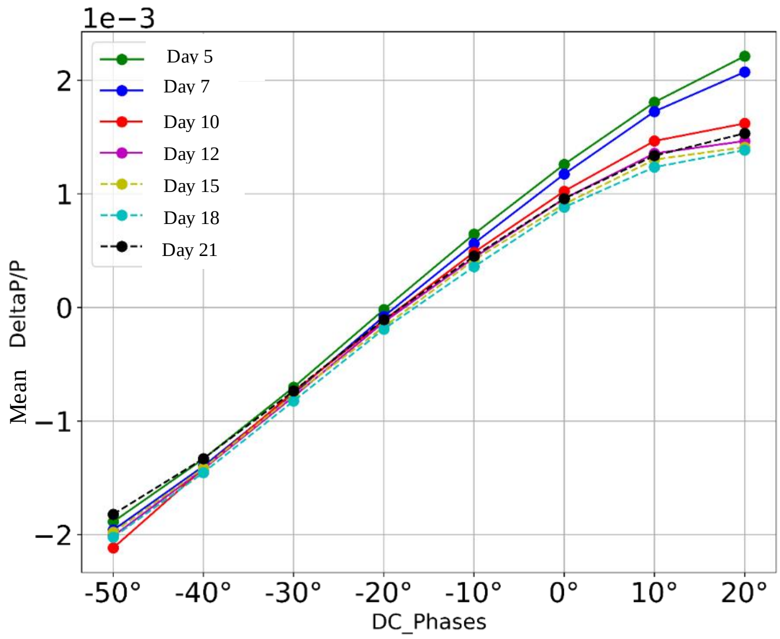

Figure 25: Mean of 129 μg/cm² foil over a span of DC phases

Next, is to find the statistical sigma or also known as the width of each energy scan distribution over time w.r.t the Debuncher cavity phases. The below figure 26 shows the statistical sigma plot with the DC phases on x-axis and Sigma Δp/p on y-axis. It is observed from the plot starting from the lower Debuncher cavity phases at -50°, -40° and -30° the difference in the sigma of the energy distribution between day 1 and day 21 accounts to 9% change whereas for the higher Debuncher cavity phases of 0°, 10°, 20° the difference in sigma over time accounts to a change of 20%, 30% & 35% respectively. The main reason behind the increase of variable change in sigma over time at higher debuncher cavity phases (between 0° and 20°) upon compared to the lower Debuncher cavity phases (between -50° and -40°) is due to development of large low energy tails over time at the higher phases leading to an increase in width of the energy distributions indicating the degradation of the stripper foil. Moreover, as the foil gets older there is a significant upward shift in sigma Δp/p value at the higher DC phases mainly above -10° and reaching a value of $1.35e^{-3}$ at the DC phase of 20° on day 21 where the stripper foil is broken. This value of $1.35e^{-3}$ is determined as the threshold limit for sigma due to the breakage of the foil and also it is foreseen that the performance of LEIR machine is limited, leading to intensity degradation of the machine. With this information it is valid that the degradation and aging of the foil is classified through the above analysis. In order to cross check and reverify the threshold value of sigma resulting from the energy distribution over time at the Debuncher cavity phase of 20°, a similar study has been made on a new foil with density of 129 $\mu g/cm^2$ from day 1 until the day it is broken. The analysis of the new foil is discussed below in detailed manner with the help of plots.

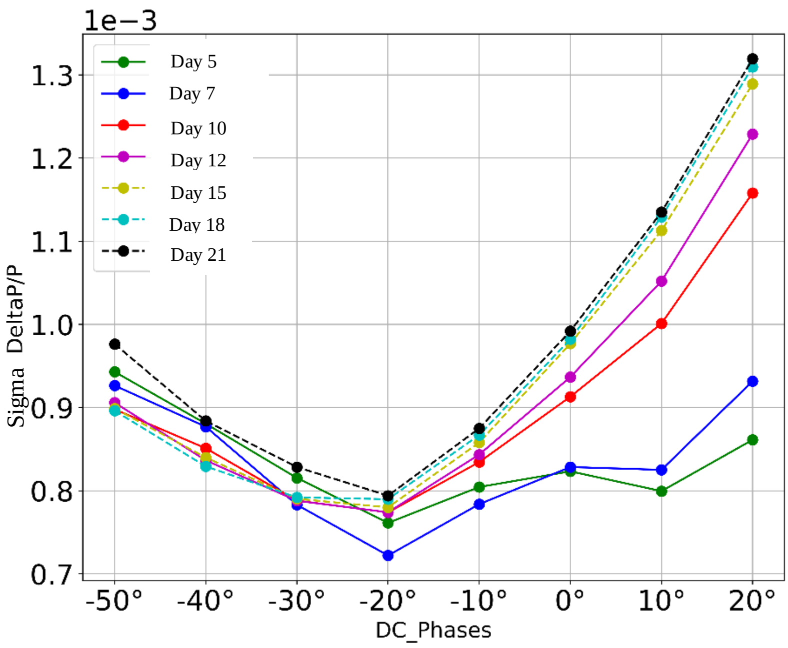

Figure 26: Sigma of 129 μg/cm² foil over a span of DC phases

Similar measurements are performed on a new 127 $\mu g/cm^2$ foil from day 1 till day 21 where the foil is broken. Energy scans are performed by setting the Ramping cavity to a flat phase of 20°, setting Debuncher cavity to a flat phase of 0° and the following results are plotted in below figure 27. It can be clearly seen from the plot that there is the development of low energy tails over time with an increase in the width of the energy distribution as the foil is getting older and thus following the same trend when compared with the analysis performed on 129 $\mu g/cm^2$ foil which is clearly stated above. Also, it is found out that the development of the low energy tails gets larger day by day at higher Debuncher cavity phases mainly above 10°.

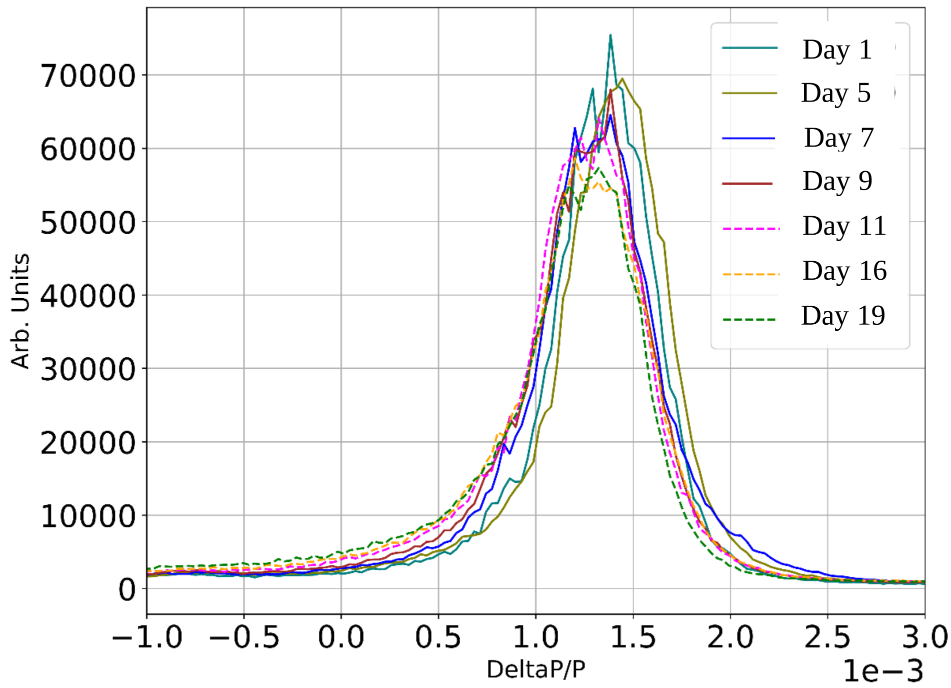

Figure 27: Measurements on 127 µg/cm² foil at RC phase of 20° and DC phase of 0°

Below figure 28 shows the statistical sigma and by looking at the DC phase of 20°, and in the similar fashion, it is again understood that as the foil gets older there is a large deviation in sigma value in terms of Δp/p and subsequently following the same trend as stated above and reaching the threshold value of 1.35e^{-3} as stated above with 129 $\mu g/cm^2$ foil. It is also observed that the change in sigma value between day 1 and day 21 at the Debuncher cavity phase of 20° accounts to 25% compared to change in sigma value of 9% at the Debuncher cavity phase of -50°.

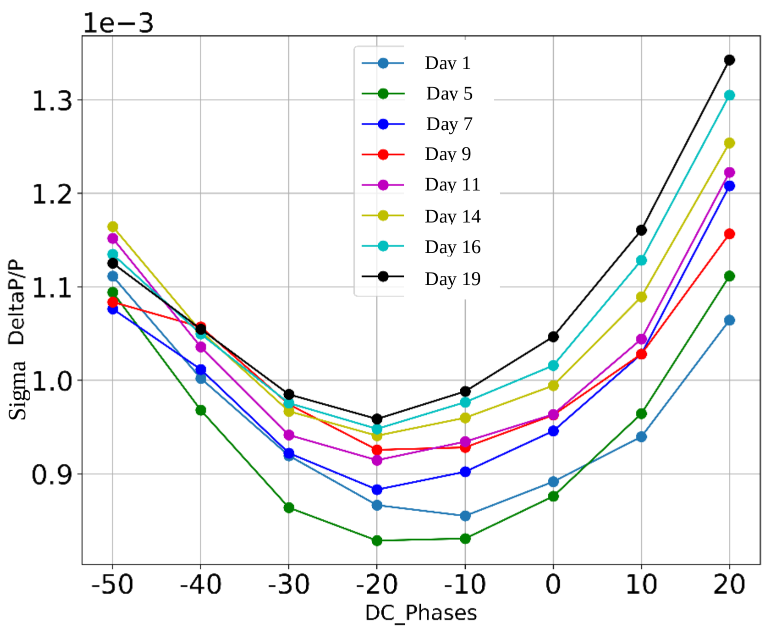

Figure 28: Sigma of 129 µg/cm² foil over a span of DC phases

4.3 Online monitoring of stripper foils

The delineated section discussed so far gives an overview on the behaviour of the stripper foils based on the measurement results performed manually on daily basis. Moving one step further the measurements performed are now automized by developing an online monitoring tool in order to study the behaviour of the foils. This tool is developed for the first time in collaboration with my supervisor Dr. Nicolo Biancacci during the research period at CERN. The main function of this online monitoring tool is to collect the data automatically in real time on an hourly basis that relieves us to perform the energy scans manually. In order to analyze the degradation of the stripper foils automatically, choosing the right Debuncher cavity phase for analysis is utmost important. For this monitoring tool a separate L3 MONIT (LINAC3 Monitoring) cycle is setup to perform the scans. As discussed above with the LEIR EARLY cycle and NOMINAL cycle, the L3 MONIT cycle is little bit different where the Debuncher cavity is set to particular flat phase of the user's interest for the incoming beam into LEIR with a single injection and closely monitor the behaviour of the beam. The below figure 4.12 illustrates the energy scans, mean, and sigma of the gaussian distribution performed on a 127 $\mu g/cm^2$ by placing the Ramping cavity to an operational flat phase of 20° and the Debuncher cavity to a flat phase of 20°. The DC phase of 20° is chosen for setup since at this phase the change in sigma concerning $\Delta p/p$ is seen predominantly in the above section.

From the below figure 29, the left plot shows the energy distributions with $\Delta p/p$ per millimetre on the x-axis at the operational Ramping cavity phase of 20° and Debuncher cavity phase of 20° performed automatically from time to time. The Debuncher cavity phase of 20° is considered here for automatic analysis, due to fact that there is the predominant observation in growth of low energy tails which results in large deviation in sigma over time and often providing the help in order to track and view the threshold reaching the limit point set which is explained clearly in the previous section 4.2. It is also observed from the plot that there is the trend in development of low energy tails over time which is indicated through a series of measurements performed. The right plot gives information about the statistical mean depicted in black and sigma in red. It is observed from the mean value of $\Delta p/p$ is there is a downward trend in the values over time. Parallelly, it is observed that the sigma value of $\Delta p/p$ is climbing towards the higher value over time. It is also observed from the right-side plot on the latest date that the latest sigma value is just above $1.25e^{-3}$ and reaching the degradation threshold limit value of $1.35e^{-3}$. It is predicted that the present installed stripper foil is getting degraded and could soon reach the end of its lifetime where it is needed to be replaced with a new foil. The above developed online monitoring tool can be viewed in live by clicking on this link here.

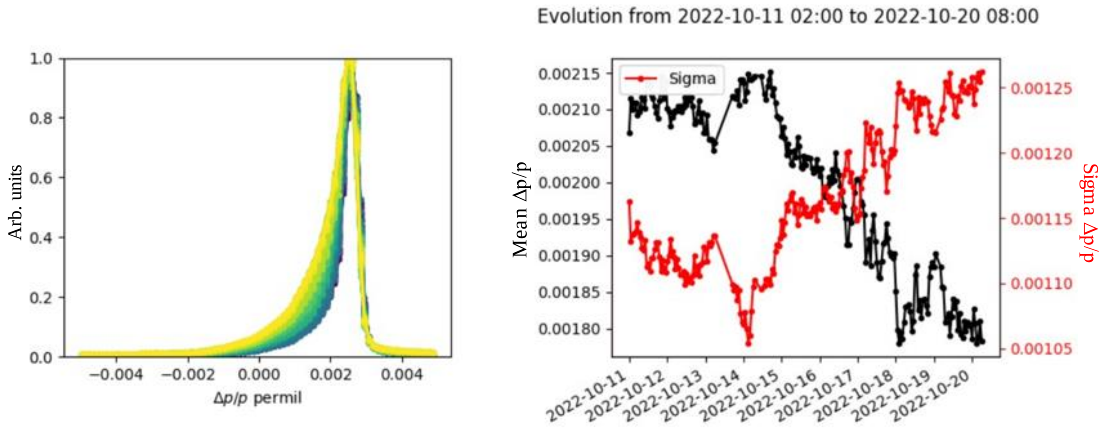

Figure 29: Hourly Energy distribution of 127 μg/cm² foil at DC phase of 20° (left), Mean and sigma plot of the distribution (right)

Chapter – 5

Conclusions

In this master thesis, firstly we had a brief introduction to the CERN accelerator complex along with the experiments being conducted at CERN and the importance of the heavy ion programme. Then the functioning overview of the main injector ion chain of accelerators which are the Linac 3 and the LEIR ring are discussed in detail in chapter 1.

In chapter 2, an introduction to the longitudinal particle beam dynamics for an ion beam is explained with the help of equations in order to understand the behaviour of the beam travelling inside an accelerator and the factors that affect the beam. Also, the momentum of particles with a six-dimensional space inside an accelerator and the resulting momentum spread or the energy spread is discussed. Next, the Linac to Filter line (ITF) which is present at the end of Linac 3 and the three main elements i.e., the stripper foil box, the Ramping cavity and the Debuncher cavity are explained in detail with the working principle of each device. The main element discussed in this thesis are the stripper foils which are responsible for producing the highly charged ions and transporting them further through the chain of accelerators. These ions reach the LHC at last and are made to collide inside the four detectors. The main working principle of the Ramping cavity and the Debuncher cavity are explained in detail which are responsible for the energy ramping and the phase space rotation of the ion beam respectively. Also, the ramped energy beam with the reduction in energy spread is seen at the end of the Linac to Stripper line.

In chapter 3, one of the main techniques that is used as a beam diagnostic system at the injection of LEIR is explained in detail. A brief introduction to the shot noise which is generated due to the random fluctuations in the number of charge carriers inside the electronic components is given. Knowing the basic theory behind the shot noise, the important concept of Schottky signals for an unbunched beam in the longitudinal plane is introduced. Next, the principles of Schottky spectrum both in time domain and frequency domain are explained in detail with the help of mathematical equations. The Schottky band or the power spectral density for N number of particles circulating inside an accelerator is given for different harmonics. This Schottky spectrum signal is measured with the support of a cascaded strip-line pickups present in LEIR making them a perfect beam position monitor. The measurements are performed and viewed through a special application known as longitudinal plane Schottky monitoring system. From the application it is possible to change the properties of the beam by varying the start and end phases of the Ramping cavity and the Debuncher cavity.

From previous chapters knowing the theoretical concept behind the stripper foils, Ramping cavity, Debuncher cavity and the Schottky signals, finally, chapter 4 describes the measurement results performed for the injected beam into LEIR using an Early cycle with a single injection pulse from LINAC3. The results were explained in two parts where in the first part the static energy scans measured on different foils with varying foil densities of 97 $\mu g/cm^2$, 127 $\mu g/cm^2$& 129 $\mu g/cm^2$ and Debuncher cavity scan between the phases of -50° to 20° is plotted. From the plot it is observed and understood that when the thickness of stripper foil increase, there is a significant shift in Δp/p. The measurement results are bench marked with the simulation results and also able to predict the energy distribution of the beam coming into LEIR well in advance. The second part of the results explained the analysis of the aging stripper foil with the foil densities of 129 $\mu g/cm^2$& 127 $\mu g/cm^2$. Firstly, foil with density of 129 $\mu g/cm^2$ at Ramping cavity phase of 20° and Debuncher cavity phase of 0° with a daily scan for two weeks is considered and plotted. It is observed that over time, as the foil gets older there is a significant shift in Δp/p and also development of low energy tails. From this observation, an innovative approach is made to analyze the degradation of the foil from the statistical mean and sigma of the beam energy distributions for all the Debuncher cavity phases. It is observed from the sigma plot that as the foil gets older, mainly above Debuncher cavity phase of -20° there is a drastic upward shift in Δp/p over time and subsequently reaching the sigma Δp/p threshold value of $1.35e^{-3}$. At this value it is observed that there is the intensity degradation of the beam in LEIR. A similar study of the aging 129 $\mu g/cm^2$ foil is seen over time with the development of low energy tails. Finally, the implementation of live online monitoring tool for evolution of the stripper foil is seen which allows to perform the energy measurements automatically, determine the sigma Δp/p threshold and depict the development of low energy tails over time.

Outlook: In future, a study will be performed to understand the development of high energy tails at lower Debuncher cavity phases and study the injection efficiency of the LEIR beam over the degradation of the stripper foils.

Bibliography

[1] C. Lefevre, "*CERN's Accelerator Complex"*, CERN-DI-0812015. 2016.

[2] M. Benedikt, et al. *"LHC Design Report, volume III"*, LHC-PROJECT-Report-810. 2004.

[3] G. Bellodi, "*Source and LINAC3 Studies"*, Proceedings of the Injector MD Days. 2017, doi: 10.23727/CERN-PROCEEDINGS-2017-002.113.

[4] C. Carli, et al. "*LEIR lattice"*. LHC-PROJECT-Report-936. 2006.

[5] C. Bal, et al. "*LEIR beam instrumentation"*. CERN-AB-2005-079. 2005.

[6] M. Chanel, "*LEIR and its transfer lines"*. LHC Performance Workshop, Chamonix, France. 2003.

[7] M. Vretenar, "*Design of the energy ramping RF system at LINAC 3"*. AB-Note-2004-068. 2004.

[8] D. Boussard, "*Schottky noise and beam transfer function diagnostics"*. CERN-SPS-86-11-ARF. CERN, 1986

[9] S. Meer, "*Diagnostics with Schottky noise. Frontiers of Particle Beams; Observation, Diagnosis and Correction"*. Springer, Berlin, Heidelberg, 1989.

[10] Tan, J., and G. Tranquille. "*Beam diagnostics with Schottky noise in LEIR"*. LHC-PROJECT-Report-982, 2006.

[11] Tan, J. "*Experimental results from LEIR Schottky system"*. CERN-AB-Note-2008-013, 2008.

[12] F. Caspers, "*Schottky signals for longitudinal and transverse bunched-beam diagnostics"*. CAS - CERN Accelerator School: Beam Diagnostics, pp.407, 2009, doi: 10.5170/CERN-2009-005.407

[13] E. Wanvik, "*Real-Time Schottky Measurements in the LHC"*. Diss. Norwegian U. Sci. Tech., 2018.

[14] N. Biancacci et al., "*LINAC3, LEIR and PS Performance with Ions in 2021 and Prospects for 2022".* Proceedings of the 13th International Particle Accelerator Conference, vol. IPAC2022, 2022, doi:10.18429/JACOW-IPAC2022-WEPOPT055.

[15] R. Scrivens, "LINAC3 ramping tracking code", GitLab repository, 2021, https://gitlab.cern.ch/scrivens/LINAC3_ramping/-/tree/master/LINAC3_ramping

[16] The LEIR Accelerator https://be-dep-op-leir.web.cern.ch/content/leir-machine

[17] S. Hirlaender et al., "*Studies of the injection and cooling efficiency in LEIR using the Longitudinal Schottky spectrum*". Proceedings of the 9th International Particle Accelerator Conference, vol. IPAC2018, 2018, doi:10.18429/JACoW-IPAC2018-TUPAF036